

1
2
3
4
5
6
7
8
9
10
11
12
13
14
15
16

Application of Parametric Speakers to Radio Acoustic Sounding System

by

Ahoro ADACHI¹ and Hiroyuki HASHIGUCHI²

¹Meteorological Research Institute, Japan Meteorological Agency

1-1 Nagamine, Tsukuba, Ibaraki 305-0052, Japan

² Research Institute for Sustainable Humanosphere, Kyoto University

Gokasho, Uji, Kyoto 611-0011, Japan

Correspondence to: Ahoro ADACHI (aadachi@mri-jma.go.jp)

Tel: +81-29-853-8584 / Fax: +81-29-856-0644

Paper re-submitted on 1 August 2019 to:

Atmospheric Measurement Techniques

17

18 **Abstract**

19 In this study, a wind profiler with radio acoustic sounding system (RASS) and
20 operational radiosonde measurements were used to investigate the technical
21 practicability and reliability of using parametric speakers to measure the vertical profile
22 of virtual temperature. Characteristics of parametric speakers include high directivity
23 and very low sidelobes, which are preferable for RASS, especially those operating at
24 urban areas. The experiments were conducted on fine days with light winds to mitigate
25 the effects of the horizontal and vertical components of wind on acoustic waves used for
26 RASS. The results of this study indicated that, although parametric speaker RASS is
27 susceptible to horizontal winds due to the narrower acoustic beam, bias and standard
28 deviation of parametric speaker RASS versus radiosonde virtual temperature difference
29 (0.1°C , 0.4°C) were close to that from acoustic speakers (0.0°C , 0.4°C). In addition,
30 when compared with acoustic speaker RASS, the values for the parametric speaker
31 RASS were even smaller (0.1°C , 0.2°C). Based on these results, it is concluded that the
32 parametric speaker RASS has accuracy and precision comparable with acoustic speaker
33 RASS despite its high directivity of sound.

34

35 **1 Introduction**

36 Accurate measurements of temperature are essential in weather forecasting and studies
37 of atmospheric dynamics at all scales. The radio acoustic sounding system (RASS) is a
38 ground-based remote sensing technique that provides vertical profiles of virtual
39 temperature from a few hundred meters above the surface up to several kilometers in
40 elevation (Marshall et al., 1972; Peters et al., 1985). RASS technique has been applied
41 to wind profilers, whereby vertical profiles of virtual temperature can be measured with
42 the same temporal and spatial resolution that the profiler uses to measure winds (e.g.,
43 Adachi et al., 2005) with a relatively high degree of reliability (Matuura et al., 1986;
44 Moran et al., 1991; Angevine and Ecklund, 1994).

45 When using RASS techniques, one or more acoustic sources are co-located with
46 an antenna, and the profiler provides the vertical profile of the speed at which the
47 acoustic disturbance propagates vertically (Angevine et al., 1994) from the
48 measurement of Doppler spectrum. RASS temperature measurements can be obtained
49 on the basis of the relationship between the virtual temperature T_v (°C), the local speed

50 of sound C_a (m s^{-1}) and the measured radial wind speed w (m s^{-1}), and a good

51 approximation can be obtained by

$$52 \quad T_v = \left(\frac{C_a - w}{20.047} \right)^2 - 273.15. \quad (1)$$

53 Thus, a vertical profile of the speed of sound can be converted to a profile of virtual

54 temperature. The radial wind speed is considered in Eq. (1) because the neglect of the

55 wind velocity along the beam is the largest source of error in RASS measurements (e.g.,

56 May et al., 1989; Angevine et al., 1994). However, we do not consider the radial wind

57 speed in our experiments, because strong clutter sometimes contaminates the Doppler

58 spectrum and masks the atmospheric echo in the vertical beam observation. This issue is

59 addressed in later sections.

60 The systematic error or bias of the virtual temperature measurements from RASS

61 observations have been shown to be less than 1°C , while the standard deviation or

62 precision has also been reported around 1°C . May et al. (1989) compared virtual

63 temperatures obtained from 915 and 50 MHz RASS with those obtained from

64 radiosonde measurements. The RASS data was averaged over approximately 6 min, and

65 about 50 soundings covering both the summer and winter seasons were examined. Both

66 the bias and the standard deviation were about 1°C, even without the application of the
67 vertical velocity correction. On the other hand, Martner et al. (1993) assessed the
68 performance of 915, 404 and 50 MHz wind profilers with RASS by comparing with
69 about 150 radiosonde measurements. They found that the bias (standard deviation) was
70 less than 0.3°C (about 1°C) for most systems, even though they did not make the
71 correction for vertical air motions, as the comparison was made under low vertical wind
72 conditions. Moran and Strauch (1994) compared temperature profiles obtained using a
73 VHF wind profiler with RASS with those obtained from radiosondes during a 5-week
74 period. They reported that the accuracy (standard deviation) was 0.9°C (less than 1°C),
75 after the application of the vertical velocity correction. Moreover, Angevine et al.
76 (1998) compared the virtual temperature measured by a 915 MHz wind profiler with
77 RASS with *in situ* observations at 396 m AGL on a tower. They found that the precision
78 of the RASS measurements was less than 0.9 K after the application of the vertical
79 velocity correction and corrections for thermodynamic constants. In addition, Görsdorf
80 and Lehmann (2000) reported that the bias (standard deviation) of the RASS
81 measurements with a 1.3 GHz wind profiler is 0.1K (0.7K) from the data observed for a

82 year compared with radiosondes if accurate corrections for vertical velocity, range, and
83 thermodynamic constants are applied. On the other hand, the height coverage of RASS
84 depends on the radio wave frequency deployed (May et al., 1988; Martner et al., 1993)
85 but is also limited by both the advection of the sound wave with the horizontal wind and
86 the atmospheric attenuation of the acoustic signal in addition to the effects of turbulence
87 and vertical temperature gradients (Lataitis, 1992).

88 A wind profiler with RASS has been frequently used to study the dynamics of the
89 atmosphere, especially in the boundary layer (e.g., Neiman et al., 1992; Peters and
90 Kirtzel, 1994; May, 1999; Bianco and Wilczak, 2002; White et al., 2003; Adachi et al.,
91 2004; Hashiguchi et al., 2004; Chandrasekhar Sarma et al., 2008). Among the
92 limitations of this method, an important one is the emission of strong sound waves,
93 whose frequency cannot be arbitrarily selected, but determined by the wavelength of the
94 radio wave used by the profiler to match the Bragg condition (the acoustic wavelength
95 λ_a is equal to half the electromagnetic wavelength λ_e). Although the acoustic speakers
96 used for RASS measurements are usually co-located with the antenna and directed
97 vertically so that the generated sound wave propagates along the radio wave, a large

108 portion of the sound wave leaks horizontally because of the sidelobes of the speakers,
109 which prevents the temporal and/or continuous operation of RASS in urban
110 environments (Wulfmeyer et al., 2015). Thus, a new type of speaker that has extremely
111 low sidelobes would be ideal for RASS measurements.

112 A theoretical study of parametric speakers (or parametric acoustic array, PAA)
113 was established by Westervelt (1963). That study revealed that the nonlinear interaction
114 between two collimated high-frequency sound beams in an ideal fluid medium produces
115 two new waves with a sum and difference frequencies, and the latter may be used to
116 produce narrow beams of sound at relatively low frequencies in the audible range.
117 Berkta and Leahy (1974) presented a theoretical description that can be used to
118 compute the far field response of a parametric array for multiple sets of parameters.
119 Thereafter, the use of parametric arrays underwater has been the subject of a number of
120 theoretical and experimental studies. On the other hand, an experimental investigation
121 of the parametric array in air was first demonstrated by Bennett and Blackstock (1975),
122 and recently, the parametric loud speaker has become available for audio and speech
123 applications (Gan et al., 2012). The properties of parametric speakers include high

114 directivity and very low sidelobes, which are preferable for RASS measurements.
115 However, to the best of our knowledge, there are few, if any, studies on RASS
116 techniques using this type of speaker.

117 In this study, a detailed evaluation of the parametric speaker for RASS
118 measurements was conducted by comparing temperature data derived from this type of
119 speaker and those from both radiosonde and acoustic speaker RASS at the
120 Meteorological Research Institute (MRI) field site in Tsukuba, Japan. Instrumentation
121 and data analysis techniques are presented in Section 2. Results are presented in Section
122 3 and discussed in Section 4. Finally, a summary of our conclusions are presented in
123 Section 5.

124

125 **2 Instrumentation and data analysis techniques**

126 The MRI wind profiler, a four-panel LAP-3000 with RASS (Fig. 1a), is the type
127 originally developed at the National Oceanic and Atmospheric Administration (NOAA)
128 Aeronomy Laboratory (Carter et al., 1995; Ecklund et al., 1988). The profiler used in
129 this study operated at 1357.5 MHz with 100 m pulse lengths and a minimum
130 (maximum) gate of 200 m (1300 m) from the antenna in RASS mode. The vertical

131 resolution was set to 100 m based on the requirements for the Global Climate Observing
132 System (GCOS) Reference Upper-Air Network (GRUAN) by the WMO (2007). The
133 effect of the vertical air motion was not considered for RASS measurements in the
134 experiments because strong clutter caused by automobiles on a nearby highway
135 sometimes contaminated the Doppler spectrum and masked the atmospheric echo
136 (Adachi et al., 2004). Indeed, the vertical velocity correction can decrease the accuracy
137 of RASS in situations with calm wind and a lower reliability of vertical wind
138 measurements (Görsdorf and Lehmann 2000).

139 The configuration and operating parameters of the wind profiler with RASS are
140 summarized in Table 1. The antenna of the profiler was co-located with four acoustic
141 speakers in cylindrical enclosures and a parametric speaker, which was mounted on top
142 of a shed (Fig. 1a). For the experiment purpose, the RASS measurements were made
143 continuously for about an hour without wind observations. Since the wind profiler
144 operated at 1.3 GHz, the frequency of the acoustic source for the RASS measurement
145 was set at about 3 kHz to match the Bragg condition. Prior to every experiment, an
146 acoustic wave with a wide frequency range (2715 to 3265 Hz corresponding to about

147 $\pm 50^\circ\text{C}$) was generated to detect center Doppler frequency of the RASS echo. Then,
148 during each experiment, the emitted acoustic frequency range was automatically
149 narrowed down to a shorter frequency span (130 Hz, corresponding to about $\pm 12^\circ\text{C}$)
150 around the detected center frequency to increase SNR and height coverage. The
151 frequency sweeps were randomly shuffled within each frequency range to make
152 acoustic spectrum almost uniform (Angevine et al., 1994).

153 The MRI parametric speaker, 100FM-001, consists of an array of more than
154 10,000 piezoelectric ceramic transducers configured on a semi-circular board with a
155 diameter of 1.8 m (Fig. 1b). The transducers were divided into 278 segments, with each
156 one mounted on the hexagonal board (Fig. 1c). The FPGA modules in the speaker
157 system were used to control the phase of the signals fed into the segments to generate
158 the acoustic beam with a particular preferred width and direction like other PAAs (e.g.,
159 Wu et al., 2012). The configuration and operating parameters of the speaker are
160 summarized in Table 2.

161 One of the desirable features of the PAA for RASS measurements is high
162 directivity of the sound beam. Prior to the designing of the MRI PAA, we made a

163 preliminary field sensitivity test for RASS using a prototype PAA with a beam width
164 smaller than 2° and relatively small power, but no RASS echo was observed. We
165 modified the prototype to broaden the beam width to about 6° or more, and the RASS
166 echo was observed up to a few range gates. We concluded that too narrow a beam is not
167 good for the RASS observation, and the PAA beam width should match that of the
168 profiler radio wave. Because the beam width of the MRI profiler is less than 7° (Table
169 1), the default sound beam width of the speaker was designed to be 5° (Table 2).
170 Although the latter width is somewhat smaller than that of the former, the RASS focal
171 spot determined by the sound beam width may be broadened by turbulence (Lataitis,
172 1992) and match the radio beam width, which is preferable for RASS measurements.

173 In order to measure the audible sound pressure level (SPL) pattern, we installed
174 the PAA on a flame (Fig. 1b) to radiate sound horizontally. The measurements were
175 made on fine (=no rain) days under calm wind (<2 m/s) with a sound level meter set at a
176 distance of 25 m, because a range of 10 m would be necessary to complete producing
177 audible sound from ultrasound with a PAA of this size (Prof. Kamakura, 2018, personal
178 communication). Safety was also considered for the level-meter operators in

179 determining the distance, as is discussed later. The PAA was installed on top of a shed
180 after the measurements (Fig. 1a). The audible sound pressure level (SPL) pattern (Fig.
181 2) measured in the field indicated that the PAA exhibited high directivity and low
182 sidelobes, as expected; the SPL was less than 55 dB (dBA) at a zenith angle of 40°,
183 which was close to the value of the background noise level of 50 dB despite the fact that
184 the peak power (100 dB) was close to that of an acoustic speaker (105 dB). By contrast,
185 for the acoustic speaker, the SPL was as high as 70 dB even at a zenith (elevation) angle
186 of 85° (5°) and is therefore significantly more annoying to the ear than a PAA.

187 To evaluate the parametric speaker for RASS measurements, temperature data
188 derived from the PAA-RASS were compared with values derived both from radiosonde
189 and from the acoustic speaker RASS. The dwell time for each RASS measurement was
190 set at about 57 s followed by an intermediate cessation operation time of 3 s, in which
191 the two speaker systems were alternately switched every minute for comparison. Each
192 RASS data set obtained with the two speaker systems was independently processed with
193 quality control to confirm the consistency in the height and time field values.

194 The profiles of virtual temperature derived from operational radiosonde
195 measurements were used as the standard reference data for comparison. The
196 radiosondes (the Meisei RS-11G used until September 2017, followed by the Meisei
197 iMS-100; Kizu et al., 2018) were launched from the Aerological Observatory, which is
198 located about 400 m northeast of the profiler (for the layout of the relative locations, see
199 Adachi et al., 2004). The time resolution of the radiosonde data used for the comparison
200 was 1 s, which corresponded to the height resolution of about 6 m. The radiosondes
201 were launched operationally at 08:30 JST (Japan Standard Time: JST=UTC+9 h), and
202 most of the RASS experiments included the launch time (Table 3). The RASS data were
203 taken during morning hours, on fine (= no rain) days, with light winds ($< 3 \text{ m s}^{-1}$ at 20
204 m AGL), mostly in autumn, when the region was under the influence of a high-pressure
205 system, which may be preferable for the formation of inversion layer. In the radiosonde
206 comparison, the RASS data were averaged over about an hour for each experiment to
207 mitigate both the effects of vertical velocity (Angevine and Ecklund, 1994; G6rsdorf
208 and Lehmann 2000) and the spatial difference between the radiosonde and the profiler
209 with RASS. Using the hourly mean may also reduce the daytime downward bias (e.g.,

210 Görsdorf and Lehmann 2000; Adachi et al., 2005), which could be attributable to
211 insects or hydrometeors that are undetectable (Angevine, 1997). Contrastingly, the 1
212 min raw RASS data were used to compare the two speaker systems.

213

214 **3 Results of comparison**

215 **3.1 Applicability of parametric speaker to RASS**

216 As there are few, if any, studies on RASS using parametric speakers, preliminary
217 experiments were first conducted to confirm whether the secondary audible waves
218 produced by this type of speaker can propagate long distances along the radio wave
219 while satisfying the Bragg condition before evaluating it for RASS application. The
220 MRI PAA radiates bifrequency primary waves that are around 37 kHz and 40 kHz from
221 all the transducers simultaneously to generate the parametric sound of the secondary
222 difference frequency, which was around 3 kHz for RASS. Since sound absorption
223 generally increases with frequency, the ultrasound may be substantially dissipated as
224 altitude increases, although the peak SPL of the ultrasonic sound close to the PAA
225 (Table 2) was about 100 dB larger than that of audible sound generated by the acoustic

226 speaker (Fig. 2). The atmospheric absorption is a function of the sound frequency,
227 temperature, humidity, and pressure of the air (ISO, 1993). Example profiles of the
228 sound attenuation coefficient and attenuation at 3 kHz and 40 kHz derived from
229 radiosonde measurements are shown in Fig. 3. In the derivation, only the effect of
230 atmospheric absorption related to viscosity and thermal conductivity of the air,
231 molecular relaxation of rotation, and vibration of O₂ and N₂ was considered (see
232 Appendix), and other physical effects (e.g., reflection from the surface; ISO, 1996) were
233 disregarded. Figure 3a shows that the attenuation for the audible wave of 3 kHz
234 propagating from the surface to an altitude of 1 km above ground level (AGL) was 14.7
235 dB, which indicated that the sound wave at this frequency with an SPL of 105 dB on the
236 ground decreased to 90.3 dB at this altitude. By contrast, this figure also suggests that
237 the sound wave at 40 kHz with an SPL of 200 dB generated on the ground was reduced
238 to less than 0 dB at 160 m AGL. Thus, the primary wave of the PAA was not expected
239 to reach beyond this altitude. However, the difference-frequency component could
240 propagate to a higher altitude because it was audible sound.

241 Figure 4 shows a set of spectra obtained with the acoustic speakers and the PAA
242 at the time when the radiosonde measurement in Fig. 3 was made. The plots were
243 obtained by the LAP-XM, which is a software program developed on the basis of the
244 Profiler On-line Program (POP; Carter et al., 1995). The RASS echoes associated with
245 the acoustic speakers were obtained from altitudes as high as 1.3 km AGL. On the other
246 hand, those associated with the PAA reached an altitude of 1.1 km AGL. Although the
247 PAA-RASS height coverage was somewhat lower than that associated with acoustic
248 speakers, this was much higher than the altitude where the primary ultrasound waves
249 were expected to dissipate. This result suggests that the secondary difference-frequency
250 component may reach the altitude comparable with the audible wave generated by
251 acoustic speakers while satisfying the Bragg condition and propagating along the radio
252 wave as an audible wave. The height coverage of the two speaker systems are discussed
253 later.

254 Another conformity of the secondary audible wave formed by the PAA to the
255 sound wave by the acoustic speaker for the RASS measurement can be seen in the
256 vertical profiles of the received echo power. Samples of the RASS echo power profiles

257 are shown in Fig. 5, along with profiles of radiosonde wind speed and horizontal
258 displacement of the sound beam center for RASS from that of the radio wave. The
259 samples were selected from the days (Table 3) when surface winds were light ($< 2 \text{ m}$
260 s^{-1}) except on 19 October (Fig. 5a). The displacement of the sound wave with horizontal
261 wind was estimated by acoustic ray tracing based on radiosonde measurements. In this
262 estimation, the sound speed was estimated using Eq. (1), assuming a stationary
263 atmosphere, in which the virtual temperature was obtained from the radiosonde data,
264 and the initial displacement of the PAA from the profiler antenna on the ground was set
265 at 4 m (Fig. 1a). The RASS echo power shown here is a relative value, not absolute,
266 because the profiler is not calibrated for received power.

267 The RASS echo power of both speaker systems decreased with altitude except for
268 the first range gate. The reason for the decrease may include atmospheric attenuation of
269 the acoustic signal and displacement of the acoustic wave from the radar antenna by the
270 wind (Lataitis, 1992), as shown by the displacement profiles (Fig. 5). The echo power
271 with the acoustic speakers was almost always larger than that of the PAA (Figs. 5a–5d).
272 This could be explained by the acoustic speaker's larger peak power than that of the

273 PAA (Fig. 2), and the integrated peak power of the acoustic system, which comprises
274 four speaker units (Fig. 1), could be much larger. The echo power with the PAA was
275 slightly larger than that of the acoustic speakers at the first gate in Fig. 5a. This could be
276 because the sound from the PAA was advected above the antenna as shown by no
277 displacement at that height in the figure, suggesting that acoustic ray tracing was
278 reliable. The estimation of RASS echo power (e.g. Adachi et al., 1993) was beyond the
279 scope of this study. However, the echo power with both speaker systems in light-wind
280 conditions (Figs. 5b–5d) decreased almost linearly (in dB) with altitude above the first
281 gate, and the difference in the gradient between the two systems was relatively small
282 (less than 15 % on average), although this small difference may also be attributable to
283 the wind. From the facts mentioned above, we concluded that the secondary audible
284 waves formed by the PAA can propagate over a long distance along the radio wave
285 while satisfying the Bragg condition and are applicable to the RASS measurements as
286 the sound wave generated by the acoustic speaker.

287 Since the PAA was shown to be applicable to the RASS measurements, we next
288 explored the reliability of the PAA-RASS measurements by comparing with radiosonde

289 observations. It is noteworthy, however, that in Fig. 5a, the echo power with the PAA
290 decreased with altitude more sharply than that associated with the acoustic speaker at
291 altitudes between 300 and 700 m AGL, where relatively high winds were observed,
292 despite the fact that the PAA-RASS echo reached the highest range gate (1300 m AGL)
293 as the acoustic speaker RASS. This suggests that the PAA has enough peak power to
294 reach the highest range gate but is more susceptible to high winds than the acoustic
295 speakers. Thus, the effect of wind on the PAA-RASS measurements is discussed later in
296 this paper.

297

298 **3.2 Comparisons with radiosonde**

299 Profiles of virtual temperature (T_v) derived from radiosonde, the PAA-RASS, and the
300 acoustic speaker RASS observations are shown in Fig. 6 along with the corresponding
301 statistics for the data. The RASS data were averaged over approximately an hour. The
302 radiosonde data were smoothed by 100 m running mean to match the RASS
303 observations. The running mean may also play a role in mitigating the effect of the
304 temperature fluctuation due to turbulence on the radiosonde measurements. The T_v
305 derived from the radiosondes was in good agreement with the RASS measurements

306 derived from both speaker systems, lying within the error bar of most of the range gates.
307 In addition, T_v derived with both speaker systems were close to each other. However,
308 bias and standard deviation tended to be large at inversion layers and at the first gate
309 (e.g., Figs. 6a, 6b, and 6c), the latter of which may corresponded to the smaller received
310 power at that gate as shown in Fig. 5. This could be attributable to the fact that the first
311 gate is too close to the antenna, and factors including the recovery of the receiver and
312 incomplete overlapping of the electromagnetic and acoustic beams due to the special
313 separation between the antenna and speaker systems could lead to a significant gradient
314 in the receiving power at this gate (Lataitis, 1992). In addition, a range error (e.g.,
315 Angevine and Ecklund, 1994; Görsdorf and Lehmann, 2000; Johnston et al., 2002)
316 caused by the height variation of the backscatter intensity may also contribute to the
317 smaller received power. It is noteworthy that the most of the highest range gates
318 correspond to a received RASS echo power of about -10 dB for both speaker systems in
319 Figs. 5 and 6, suggesting that the received power is one of the factors determining the
320 height coverage, although factors that determine the received power including the sound
321 attenuation may be different for each system.

322 Scatter diagrams comparing radiosonde virtual temperature with that from
323 RASS for all experiments are shown in Fig. 7 along with statistics. The first range gate
324 data of the RASS measurements were not considered because they are less reliable. This
325 figure shows that both the PAA and acoustic speaker RASS measurements of virtual
326 temperature were generally in good agreement with those derived from radiosonde
327 measurements, as expected. The linear regressions for both speaker systems were close
328 to the one-to-one relation, and correlation coefficients were close to unity. In addition,
329 the systematic error was less than 0.1 °C and the standard deviation was 0.4°C for both
330 systems, suggesting that both systems are reliable for RASS measurements.

331

332 **4 Discussions**

333 As reported above, we found many instances in which the PAA speaker system
334 exhibited comparable performance with the acoustic speakers with respect to the RASS
335 measurements in observing profiles of the Doppler spectrum and the virtual temperature,
336 as shown in the statistics for the comparisons both with radiosonde and with the
337 acoustic speaker RASS. Indeed, the bias and standard deviation for each speaker system
338 RASS with respect to radiosonde were in good agreement with results reported in

339 previous studies (e.g., Görsdorf and Lehmann 2000), despite no correction for vertical
340 velocity, which could have been partly because of the experiments being conducted on
341 fine days with light wind and the application of a relatively long averaging time. In
342 addition, removing the first gate data from the statistics may also contribute to the
343 results.

344 Although applying a long averaging time could mitigate the effect of vertical
345 airflow on bias (e.g., Moran and Strauch, 1994), it may degrade the statistics when the
346 virtual temperature profile evolves within the duration of the RASS measurement. On
347 the other hand, the statistics also indicated that the data number associated with the PAA
348 was smaller than that of the acoustic speakers (e.g., Fig. 6), implying that the mean
349 height coverage with the former was lower than that of the latter presumably because of
350 wind in addition to the low peak power mentioned previously. Thus, we independently
351 focus our attention on both the effects of the time evolution of the temperature profile
352 on the statistics and of wind on the height coverage of the RASS measurement in the
353 following sections.

354

355 **4.1 Effect of rapid time evolution of temperature profile**

356 In the comparisons, the RASS data were averaged for a relatively long time to minimize
357 the effects of both vertical velocity and the spatial difference between the radiosonde
358 and the profiler with RASS. However, the temperature profiles derived from radiosonde
359 observations may not be well suited for use as standard reference data if the temperature
360 profile evolved rapidly within the hour-long RASS observation duration. In the
361 experiments, since the operational radiosondes were launched in the morning of fine
362 days, an inversion layer was frequently observed (Fig. 6) as expected. In fact, 12
363 inversions including multiple inversion layers (e.g., Fig. 6b) were observed in 8 of the
364 16 experiments. Inversion layers can evolve in a relatively short time due to surface
365 heating and cooling and/or the development of the boundary layer in the morning.
366 Indeed, the surface virtual temperature increased by 2.3°C on average with a standard
367 deviation of 1.0°C within an hour for the experiments shown in Fig. 6. Thus, the
368 temperature profile measured with the radiosonde can differ from the mean temperature
369 profile obtained from RASS even though both measurements represented an actual
370 profile, which may result in degrading the statistics for the RASS evaluation.

371 A sample of the temperature profile observing an inversion layer is shown in Fig.

372 8. This observation was made more than 3 h after sunrise (05:15 JST) on that day. The
373 *T_v* profiles with error bars were the mean RASS measurements averaged over an hour
374 from acoustic (red) and PAA (blue) speakers. Both RASS profiles represented the
375 radiosonde profile to some extent but did not follow the profile well, especially around
376 the inversion layer. The large standard deviations indicated by long error bars may
377 reflect the time evolution of the temperature profile in addition to the measurement
378 precision of RASS. By contrast, the 1 min raw RASS data recorded around the
379 radiosonde launch time represented the inversion layer better than the mean RASS
380 measurements at some points, although there were still some discrepancies, which may
381 have been due to the locality of the inversion layer, the effects of vertical air motion or
382 turbulence, or the time difference between RASS and radiosonde in addition to the
383 accuracy and precision of the RASS measurements. The discrepancy above the
384 inversion layer may be caused by the locality of the temperature, because the MRI
385 observation field covered by vegetation (Adachi et al., 2005) ends about 500 m from the
386 profiler, which corresponds to the horizontal displacement at that height. On the other
387 hand, the discrepancies in and below the inversion could be mitigated by considering

388 the effect of the vertical airflow and/or applying a range correction. In terms of the time
389 difference, it is noteworthy that the radiosonde measurement is not a snapshot but
390 sequential; it took more than 2 min for the radiosonde to ascend to an altitude of 800 m
391 AGL, and the temperature profile may evolve even during this time. Thus, a comparison
392 with measurements that have both small spatial difference and high time resolution is
393 needed to evaluate the PAA-RASS measurement.

394

395 **4.2 Comparison with acoustic speaker RASS**

396 To suppress the effects of the spatial and time difference between the two
397 platforms on the evaluation, we next compared the temperatures derived from the
398 PAA-RASS with that from the acoustic speaker RASS. Of course, this comparison does
399 not provide an absolute but relative evaluation of the PAA-RASS measurement. This
400 issue should be kept in mind in examining the intercomparisons presented in this
401 section. In the intercomparison, the requirements for high-quality upper-air reference
402 data (bias $\leq 0.1\text{K}$, $\sigma \leq 0.2\text{K}$) proposed by WMO (2007) for the GRUAN were used as
403 criteria for the evaluation, although they are not for virtual temperature but for real
404 temperature.

405 A normalized frequency diagram and scatterplot of virtual temperature obtained
406 by the acoustic speaker RASS versus the PAA-RASS are shown in Fig. 9. The 1 min
407 raw data obtained alternately are presented in Fig. 9a, whereas the data averaged for
408 about an hour are plotted in Fig. 9b. Figure 9a shows that the PAA-RASS
409 measurements of virtual temperature were generally in good agreement with those of
410 the acoustic speaker RASS despite disregarding the time difference in the two systems.
411 The linear regression line was close to the one-to-one relation, and the correlation
412 coefficient was close to unity. Moreover, the mean bias and standard deviation of the
413 difference between the two speaker systems were less than 0.1°C and close to 0.4°C ,
414 respectively, which are comparable with those obtained by the comparison with
415 radiosonde (Fig. 7) despite the higher time resolution. Since the spatial difference was
416 negligible and the time difference was quite small, the reason for this discrepancy could
417 include temperature fluctuation due to turbulence. Indeed, the mean (max and min)
418 increase of the virtual temperature at the surface for all the experiments was
419 $0.2 \pm 0.5^{\circ}\text{C}/10 \text{ min}$ ($1.4^{\circ}\text{C}/10 \text{ min}$, $-1.3^{\circ}\text{C}/10 \text{ min}$), which suggests that temperature
420 fluctuation aloft was occurring.

421 A scatter diagram comparing the mean acoustic speaker RASS measurements
422 with those from the parametric speaker RASS is shown in Fig. 9b. The data were
423 averaged over about an hour to minimize the effect of temporal fluctuation of
424 temperature and improve the statistics. Indeed, the linear regression was close to the
425 one-to-one relation, and the correlation coefficient was closer to unity. In addition, both
426 the bias (0.06°C) and standard deviation (0.16°C) improved and satisfied the WMO
427 requirements.

428 From the evaluations mentioned above, we conclude that the accuracy and
429 precision of the parametric speaker RASS are comparable with those of the acoustic
430 speaker RASS for measuring the vertical profile of virtual temperature. The reliability
431 of the parametric speaker RASS could be improved by applying the time average over
432 the appropriate period, advanced quality control, and/or corrections for both range and
433 vertical airflow as long as the effect of the ground clutter is negligibly small.

434

435 **4.3 Effect of horizontal wind on the height coverage of the RASS measurement**

436 The reliability of the parametric speaker RASS measurement was shown to be
437 equivalent to the acoustic speaker RASS. However, we found many instances in which

438 the former tended to have less height coverage than the latter (Figs. 4, 5, and 6), which
439 may also be reflected by the fewer number of data in the statistics (Figs. 6, 7, and 8).
440 Although the parametric speaker system exhibited less peak power than the acoustic
441 speaker system, the weak power cannot be the only reason for the lower height coverage
442 because the results show that the former can observe up to the highest range gate as the
443 latter in some conditions (e.g., Figs. 5a, 5b, 6a, and 8). On the other hand, the results
444 also suggest that the reason may include the effect of wind aloft (e.g., Fig. 5a). Because
445 the acoustic beam generated by the parametric speaker is narrow, it could be susceptible
446 to the horizontal airflow, which displaces the acoustic wave from the radar antenna as
447 shown in Fig. 5. Thus, the effect of horizontal wind on the height coverage of the
448 parametric speaker RASS measurement was evaluated by comparing it with the
449 radiosonde wind data.

450 A scatter diagram comparing the mean RASS height coverage and horizontal
451 displacement of the center of the sound for RASS from that of radio wave at 1200 m
452 AGL is shown in Fig. 10, as well as the mean wind speed aloft. The horizontal
453 displacement was estimated by acoustic ray tracing. In the estimation, the initial

454 displacement of the acoustic speaker system from the profiler antenna on the ground
455 was set at 0 m, because the antenna is surrounded by the four acoustic speakers,
456 whereas that of the PAA was set at 4 m (Fig. 1a). The wind speed aloft is the mean wind
457 from 20 to 1200 m AGL (Table 3), which is the highest mean coverage of the
458 parametric speaker RASS measurements in calm wind conditions ($< 2 \text{ m s}^{-1}$) as shown
459 in the figure. The data measured on 30 November 2016 are not considered in the
460 analysis because the RASS measurement was made more than 40 min later than the
461 radiosonde observation (Table 3). Note that the mean RASS height coverage shown in
462 the figure is different from the height coverage of the mean virtual temperature profile
463 in Fig. 6, because the latter reflects the maximum height coverage within the observed
464 profiles after quality control in the duration of the RASS measurement. The long error
465 bars may reflect the large time evolution of the RASS height coverage, which may also
466 be related to the evolution of the wind in the duration.

467 The parametric speaker RASS measurements tended to reach less altitude than the
468 acoustic speaker RASS, even when the horizontal displacement is less than 10 m
469 (corresponding to a wind speed of around 4 m s^{-1}). The reason for the lower coverage

470 under small displacement (light wind) conditions may include the parametric speaker's
471 lower peak power than that of the acoustic speaker system. The height coverage
472 decreased with the displacement and/or wind speed for the parametric speaker RASS, as
473 indicated by the linear regression analysis. In contrast, when the displacement is less
474 than 16 m (corresponding to a wind speed of around 6 m s^{-1}), most of the acoustic
475 speaker RASS measurements achieved a height coverage of around 1300 m AGL,
476 which was the highest range gate for the RASS measurement (Table 1). This suggests
477 that the acoustic speaker RASS keeps on observing at a high altitude even in relatively
478 high wind conditions, as also indicated by the short error bars.

479 It is noteworthy, however, that the height coverage of RASS with acoustic
480 speakers drops sharply to 1000 m AGL at a horizontal displacement of 15–16 m and
481 exhibits a tendency to decrease with the displacement afterward as the parametric
482 speaker RASS. By contrast, the height coverage of the parametric speaker tends to
483 decrease monotonically with the displacement at almost all ranges. These results
484 suggest that the parametric speaker RASS is more sensitive to wind because of the
485 narrow beam, whereas the acoustic speaker RASS is surprisingly robust. Since the four

486 acoustic speakers were not adjusted in phase, this robustness could be explained by the
487 higher aggregate sound power than that shown in Fig. 2 and possible location of sound
488 wave above the antenna in spite of relatively high winds.

489 To compensate for the lower wind tolerance, two additional experiments were
490 performed, in which the acoustic beam was broadened and steered. The parametric
491 speaker system employed for the RASS experiments was equipped with FPGA that
492 controlled the beam pattern of the sound, including beam width and direction. We
493 broadened the beam width from 5° to 12° (Fig. 2) when the parametric RASS echo was
494 observed up to an altitude of 1200 m AGL. However, this experiment resulted in a
495 decrease of the height coverage to 500 m AGL. The height coverage decrease could
496 have been due to the decrease of the peak power associated with beam broadening. In
497 fact, the measured peak power was decreased by 15 dB in our system by broadening the
498 beam (Fig. 2). Therefore, by using this technique, a parametric speaker with more peak
499 power was needed in our case to acquire equivalent height coverage with the acoustic
500 speaker system, which may result in increasing both the size and cost of the system.

501 On the other hand, the peak power does not decrease significantly with the
502 angle of the beam as long as the angle is small. The SPL pattern at multiple zenith
503 angles measured in the field is shown in Fig. 11. The peak power was decreased by
504 about 7.5 dB by reducing the power supply to the PAA amplifier, which decreased not
505 only the audible sound but also the ultrasound levels for practical reasons (noisy) and
506 measurement safety. The results indicated that the peak power decreased by only 3.8 dB
507 when the beam was steered to a zenith angle of 10° , which corresponds to a horizontal
508 wind speed of 60 m s^{-1} . The sound wave might be displaced by the horizontal wind but
509 advected to above the antenna if the wave is generated windward with an appropriate
510 zenith angle. Thus, we conducted another experiment with the acoustic beam zenith
511 angle of 2° windward on a day when a mean wind speed of about 12 m s^{-1} between 200
512 and 1200 m AGL was observed with the wind profiler. Unfortunately, no RASS echo
513 was observed, which may be partly because the sound wave did not propagate vertically
514 to the ground, and the advected sound wave front above the antenna was not normal to
515 the propagation direction of the radio wave. Additionally, the acoustic wave front may
516 have been distorted by wind shear. In that case, the radio wave might have been steered

517 to the direction normal to the sound wave front by considering the advection and
518 distortion of the sound wave front from the wind profiler measurements.

519

520 **4.4 Health effects of ultrasound exposure**

521 Since the ultrasonic SPL generated by the PAA is extremely high (>200 dB), the health
522 effects of ultrasound exposure in the area close to the PAA should be considered. In
523 studies involving small animals (WHO, 1982), mild biological changes have been
524 reported during prolonged exposure to airborne ultrasound with levels in the range of
525 95–130 dB at frequencies ranging 10–54 kHz, which become more severe with
526 increasing SPL. Thus, the PAA should not be installed on or under the ground level, as
527 it can be easily accessed by animals. Because the PAA for RASS emits sound vertically,
528 animals aloft, including birds and/or insects, can be exposed to the sound beam.
529 However, those animals are capable of avoiding the risk quite easily, because they can
530 perceive the audible sound from the PAA, and the beam width is very narrow. In fact,
531 no animals, including bugs and/or birds, died so far on the PAA after more than 100 h
532 of operation.

533 On the other hand, no adverse physiological or auditory effects appear to occur in
534 humans exposed to sound pressure levels up to about 120 dB (WHO, 1982; Health
535 Canada, 1991). At 140 dB, mild heating may be felt in the skin clefts. With increasing
536 sound pressure levels, the human body becomes warmer until death from hyperthermia
537 has been estimated to occur at levels greater than 180 dB. This lethal threshold value
538 corresponds to a distance of less than 17 m from the PAA, with an ultrasonic SPL of
539 200 dB, assuming an atmospheric attenuation of 1.2 dB m^{-1} (Fig. 3). To avoid
540 ultrasound exposure, we installed the PAA on top of a shed with a height of 2 m so that
541 the speaker won't be accessed by anyone. Moreover, rotational warning lights were
542 installed on the wall of the shed (Fig. 1d) to alert people to the emission of ultrasound
543 more than 50 dB (yellow) and/or 100 dB (red).

544

545 **5 Conclusions**

546 We investigated the applicability of parametric speakers to RASS for measuring
547 the vertical profile of virtual temperature by comparing the data with those obtained
548 from both radiosonde and the acoustic speaker RASS. In the experiments, the
549 operations of the two speaker systems were swapped every minute alternately for the

550 comparison. A detailed analysis of the profiles of both the acoustic attenuation and the
551 Doppler spectrum suggest that although the primary ultrasound generated by the
552 parametric speaker may be dissipated greatly as altitude increases, the secondary
553 audible waves generated from the bifrequency ultrasound can propagate long distances
554 while satisfying the Bragg condition.

555 We have also compared parametric speakers with both radiosonde and acoustic
556 speakers to estimate the reliability of RASS in measuring the virtual temperature (T_v).
557 The results indicated that T_v measured with parametric speaker RASS has comparable
558 reliability with the acoustic speaker RASS measurements; the bias and standard
559 deviation (0.1°C , 0.4°C) for the parametric speaker were close to those for the acoustic
560 speaker (0.0°C , 0.4°C) with respect to radiosonde, which was consistent with the results
561 reported in previous studies, although the conditions in those studies, including the
562 corrections for the vertical wind and/or range, were different from ours. We also found
563 that not only the spatial difference between the two platforms but also both the
564 evolution of the temperature profile during the RASS measurement and temperature
565 fluctuation due to turbulence could contribute to deteriorate the statistics. To mitigate

566 these effects, a comparison of virtual temperature obtained from the two speaker
567 systems was also performed. The results indicated that the bias and standard deviation
568 (0.1°C, 0.2°C) of the parametric speaker RASS were quite small and satisfied the
569 requirements for high-quality upper-air reference data proposed by the WMO (2007).
570 Taken together, we conclude that parametric speaker RASS has comparable accuracy
571 and precision with acoustic speaker RASS with respect to the measurement of the
572 virtual temperature profile.

573 We examined the height coverage of RASS and found that the parametric speaker
574 deployed in the experiments tended to have less coverage than the acoustic speakers,
575 which may be a result of the parametric speaker having high directivity, and the
576 generated sound was more susceptible to the displacement from the radar antenna by
577 horizontal wind than the sound wave by the acoustic speakers. Thus, we broadened the
578 beam width of the parametric speaker, which resulted in degrading height coverage
579 because this operation deteriorates the peak power of the audible sound. The sound
580 wave was then steered windward so that the advected sound was located above the
581 antenna. However, no echo was observed, presumably because the sound wave front

582 advected to above the antenna was not normal to the propagation direction of the radio
583 wave in the experiments. In addition, the sound wave front may have been distorted by
584 wind shear. This issue might be solved by using wind profilers that are capable of
585 steering the radio wave (e.g., Adachi and Kobayashi, 2001; Law et al., 2002; Palmer et
586 al., 2005) to the direction normal to the sound wave front as Masuda (1988) proved with
587 the MU radar (Fukao et al., 1985).

588 The results of this study including the statistics do not necessarily apply to all
589 locations, altitudes, and seasons; in particular, we note that the comparisons in this case
590 study were made in the morning on fine days with light wind when the effects of
591 horizontal and vertical wind would be less expected. This condition is possible even in
592 other seasons, but frequency is likely to be less.

593 In summary, we confirm that a parametric speaker is applicable to RASS
594 measurement with a reliability comparable with acoustic speakers. Although it is
595 sensitive to horizontal wind, this type of speaker could be installed to wind profilers
596 located in urban areas for continuous-operational observations (e.g., Ishihara et al.,

597 2006) to improve weather forecast because it has high directivity and no horizontal
598 sound wave leaks to annoy nearby residents.

599

600 *Acknowledgements.*

601 The authors wish to thank Emeritus Professor T. Tsuda of Kyoto University for many
602 helpful discussions and comments regarding the research presented and Mr. S. Hoshino
603 of the Aerological Observatory for providing information on radiosonde measurements.

604 The first author wishes to thank Mr. J. Neuschaefer of Vaisala for offering the LAP-XM
605 software to analyze the spectrum data, Prof. T. Kamakura of the university of
606 electro-communications, Mr. S. Onogi of the meteorological instrument centre, Mr. N.
607 Okushima and Mr. E. Suzuki of Starlite Co., Ltd. and Mr. T. Takai for technical support,
608 and Drs. Y. Shoji, M. Mikami, A. Segami, and S. Tsunomura of MRI for providing an
609 opportunity to conduct the experiments. The authors also thank anonymous reviewers
610 who made many helpful comments that improved this work substantially. This study
611 was partially supported by JSPS KAKENHI Grant Number 15K01273 and 17H00852.

612

613 **Appendix**

614 **Calculation of the atmospheric attenuation**

615 The method of estimating attenuation coefficient for atmospheric absorption from
616 temperature, humidity, and pressure is summarized here based on ISO 9613-1 (ISO,
617 1993). The attenuation coefficient α (dB m⁻¹) is expressed by the sum of four terms in
618 good approximation as

619
$$\alpha = \alpha_{cl} + \alpha_{rot} + \alpha_{vib,O} + \alpha_{vib,N}, \quad (A1)$$

620 where α_{cl} represents the classical absorption caused by the transport processes, α_{rot} is
621 the molecular absorption by rotational relaxation, and $\alpha_{vib,O}$ and $\alpha_{vib,N}$ indicate the
622 molecular absorption caused by vibrational relaxation of oxygen and nitrogen,
623 respectively. The molecular absorption by other compositions of the air including
624 carbon dioxide is small and neglected in the calculation.

625 The first two terms of Eq. (A1) related to the classical and rotational absorption is
626 given by their sum, α_{cr}

627
$$\alpha_{cr} = \alpha_{cl} + \alpha_{rot} = 1.60 \times 10^{-10} \left(\frac{T}{T_0}\right)^{\frac{1}{2}} \left(\frac{P_a}{P_r}\right)^{-1} f^2, \quad (A2)$$

628 where T (K) is the atmospheric temperature, T_0 is the reference air temperature (293.15
629 K), P_a (hPa) is the atmospheric pressure, P_r (hPa) is the reference air pressure (1013.25
630 hPa), and f (Hz) is the sound frequency.

631 The two vibrational relaxation terms in Eq. (A1) are given respectively by,

$$632 \quad \alpha_{vib,O} = [(\alpha\lambda)_{max,O}] \times \frac{f}{c_s} \times \left\{ 2 \left(\frac{f}{f_{rO}} \right) \left[1 + \left(\frac{f}{f_{rO}} \right)^2 \right]^{-1} \right\}, \quad (A3)$$

633 and

$$634 \quad \alpha_{vib,N} = [(\alpha\lambda)_{max,N}] \times \frac{f}{c_s} \times \left\{ 2 \left(\frac{f}{f_{rN}} \right) \left[1 + \left(\frac{f}{f_{rN}} \right)^2 \right]^{-1} \right\}, \quad (A4)$$

635 where subscripts O and N represent oxygen and nitrogen, respectively, $[(\alpha\lambda)_{max}]$ (dB
636 m^{-1}) represents the maximum attenuation by a vibrational relaxation over a distance of a
637 wavelength, λ (m), c_s ($m s^{-1}$) is the sound speed, and f_r (Hz) is the relaxation frequency.

638 The maximum attenuation by a vibrational relaxation for oxygen and nitrogen are
639 given respectively by,

$$640 \quad [(\alpha\lambda)_{max,O}] = \left(\frac{40\pi}{35} \right) (\log_{10} e) X_O \left(\frac{\theta_O}{T} \right)^2 \exp \left(-\frac{\theta_O}{T} \right), \quad (A5)$$

641

$$642 \quad [(\alpha\lambda)_{max,N}] = \left(\frac{40\pi}{35} \right) (\log_{10} e) X_N \left(\frac{\theta_N}{T} \right)^2 \exp \left(-\frac{\theta_N}{T} \right). \quad (A6)$$

643 where X_O (= 0.209476) and X_N (=0.78084) represent the standard molar concentrations
 644 of dry air, and θ_O (=2239.1 K) and θ_N (=3352.0 K) are the characteristic vibrational
 645 temperature for oxygen and nitrogen, respectively.

646 The sound speed c_s in Eq. (A3) and (A4) at a molecular concentration of water
 647 vapor of h (%) is given by

$$648 \quad c_s = c_a \times \sqrt{1 - \frac{h}{100} \left(\frac{\gamma_w}{\gamma_a} - \varepsilon \right)} = c_0 \times \sqrt{\frac{T}{T_0}} \times \sqrt{1 - \frac{h}{100} \left(\frac{\gamma_w}{\gamma_a} - \varepsilon \right)}, \quad (A7)$$

649 where C_a is the sound speed for dry air, γ_w (=1.33) and γ_a (=1.40) are heat capacity ratio
 650 for water vapor and dry air, respectively, ε (=0.662) is the ratio of the molecular weight
 651 of water vapor to the molecular weight of air, and C_0 is the sound speed for dry air at
 652 the reference air temperature, T_0 . The value of h is given from the relative humidity, h_r
 653 (%) by

$$654 \quad h = h_r \left(\frac{P_{sat}}{P_r} \right) / \left(\frac{P_a}{P_r} \right) = h_r \left(\frac{P_{sat}}{P_a} \right), \quad (A8)$$

655 where P_{sat} (hPa) is the saturation vapor pressure given by

$$656 \quad P_{sat} = P_r \times 10^{\left(-6.8346 \times \left(\frac{T_{01}}{T} \right)^{1.261} + 4.6151 \right)}, \quad (A9)$$

657 and T_{01} (=273.16 K) is the triple-point isotherm temperature. The sound speed in dry air

658 C_a is given by

659 $c_a = \sqrt{\frac{\gamma_a R}{M_d} T}$, (A10)

660 where R ($= 8.314 \text{ J mol}^{-1} \text{ K}^{-1}$) is the universal gas constant, and M_d ($=2.896 \times 10^{-2} \text{ kg}$
661 mol^{-1}) is the molecular weight for dry air. By substituting values of R , and M_d to Eq.
662 (A10), we may derive

663 $c_a = 20.048\sqrt{T}$, (A11)

664 and $C_0 = 343.25 \text{ m s}^{-1}$ at a temperature of T_0 . Note that Eq. (A11) corresponds to Eq. (1)
665 in stationary atmosphere because air temperature T is equal to virtual temperature T_v in
666 dry air.

667 The relaxation frequency for O and N are given by,

668 $f_{rO} = \left(\frac{P_a}{P_r}\right) \left(24 + 4.04 \times 10^4 h \frac{0.02+h}{0.331+h}\right)$, (A12)

669 and

670 $f_{rN} = \left(\frac{P_a}{P_r}\right) \left(\frac{T}{T_0}\right)^{-\frac{1}{2}} \times \left[9 + 280h + \exp\left[-4170 \left\{\left(\frac{T}{T_0}\right)^{-\frac{1}{3}} - 1\right\}\right]\right]$, (A13)

671 respectively.

672 By substituting Eqs. (A2) — (A11) to Eq. (A1), we may derive,

673 $\alpha \approx 8.686f^2 \left[\left\{1.84 \times 10^{-11} \left(\frac{P_a}{P_r}\right)^{-1} \left(\frac{T}{T_0}\right)^{\frac{1}{2}}\right\} + \left(\frac{T}{T_0}\right)^{-\frac{5}{2}} \times \left\{0.01275 \times \right.\right.$
674 $\left. \exp\left(\frac{-2239.1}{T}\right)\right\} \left\{f_{rO} + \left(\frac{f^2}{f_{rO}}\right)\right\}^{-1} + 0.1068 \times \exp\left(\frac{-3352.0}{T}\right) \left\{f_{rN} + \left(\frac{f^2}{f_{rN}}\right)\right\}^{-1} \right]$, (A14)

675 where f_{r0} and f_{rN} are given by Eqs. (A12) and (A13), respectively.

676 The attenuation coefficients at 3 kHz and 40 kHz as a function of temperature and
677 relative humidity estimated using Eq. (A14), is shown in Fig. A1. This figure indicates
678 that the attenuation coefficient for ultrasound at 40 kHz is larger than that for audible
679 sound at 3 kHz, as expected. In addition, the attenuation coefficient depends on the
680 temperature and humidity for both frequencies. Note that the attenuation coefficient for
681 audible sound peaks at lower temperatures ($<10^{\circ}\text{C}$) than those for ultrasound,
682 suggesting that the attenuation coefficient could increase with altitude for the former,
683 while it decreases for the latter (e.g., Fig. 3, >1 km AGL). In contrast, the contribution
684 of air pressure to the attenuation coefficient on the ground does not differ very much
685 from that at an altitude of 1100 m AGL (~ 900 hPa).

686 **References**

- 687 Adachi, A., Clark, W. L., Hartten, L. M., Gage, K. S., and Kobayashi, T.: An
688 observational study of a shallow gravity current triggered by katabatic flow, *Ann.*
689 *Geophys.*, 22, 3937-3950, doi: 10.5194/angeo-22-3937-2004, 2004.
- 690 Adachi, A. and Kobayashi, T.: RHI observations of precipitation with boundary wind
691 profiler, Munich, 2001, 116-117.
- 692 Adachi, A., Kobayashi, T., Gage, K. S., Carter, D. A., Hartten, L. M., Clark, W. L., and
693 Fukuda, M.: Evaluation of three-beam and four-beam profiler wind measurement
694 techniques using a five-beam wind profiler and collocated meteorological tower, *J.*
695 *Atmos. Oceanic Technol.*, 22, 1167-1180, doi: 10.1175/jtech1777.1, 2005.
- 696 Adachi, T., Tsuda, T., Masuda, Y., Takami, T., Kato, S., and Fukao, S.: Effects of the
697 acoustic and radar pulse length ratio on the accuracy of radio acoustic sounding
698 system (RASS) temperature measurements with monochromatic acoustic pulses,
699 *Radio Sci.*, 28, 571-583, doi: 10.1029/93RS00359, 1993.
- 700 Angevine, W. M.: Errors in mean vertical velocities measured by boundary layer wind
701 profilers, *J. Atmos. Oceanic Technol.*, 14, 565-569, doi:
702 10.1175/1520-0426(1997)014<0565:EIMVVM>2.0.CO;2, 1997.
- 703 Angevine, W. M., Bakwin, P. S., and Davis, K. J.: Wind profiler and RASS
704 measurements compared with measurements from a 450-m-tall tower, *J. Atmos.*
705 *Oceanic Technol.*, 15, 818-825, doi:
706 10.1175/1520-0426(1998)015<0818:Wparmc>2.0.Co;2, 1998.
- 707 Angevine, W. M. and Ecklund, W. L.: Errors in radio acoustic sounding of temperature,
708 *J. Atmos. Oceanic Technol.*, 11, 837-842, doi:
709 10.1175/1520-0426(1994)011<0837:EIRASO>2.0.CO;2, 1994.
- 710 Angevine, W. M., Ecklund, W. L., Carter, D. A., Gage, K. S., and Moran, K. P.:
711 Improved radio acoustic sounding techniques, *J. Atmos. Oceanic Technol.*, 11,
712 42-49, doi: 10.1175/1520-0426(1994)011<0042:IRAST>2.0.CO;2, 1994.
- 713 Bennett, M. B. and Blackstock, D. T.: Parametric array in air, *J. Acoust. Soc. Am.*, 57,
714 562-568, doi: 10.1121/1.380484, 1975.
- 715 Berktag, H. O. and Leahy, D. J.: Farfield performance of parametric transmitters, *J.*
716 *Acoust. Soc. Am.*, 55, 539-546, doi: 10.1121/1.1914533, 1974.
- 717 Bianco, L. and Wilczak, J. M.: Convective boundary layer depth: Improved
718 measurement by Doppler radar wind profiler using fuzzy logic methods, *J. Atmos.*

719 Oceanic Technol., 19, 1745-1758, doi:
720 10.1175/1520-0426(2002)019<1745:CBLDIM>2.0.CO;2, 2002.

721 Carter, D. A., Gage, K. S., Ecklund, W. L., Angevine, W. M., Johnston, P. E., Riddle, A.
722 C., Wilson, J., and Williams, C. R.: Developments in UHF lower tropospheric wind
723 profiling at NOAA's Aeronomy Laboratory, Radio Sci., 30, 977-1001, doi:
724 10.1029/95RS00649, 1995.

725 Chandrasekhar Sarma, T. V., Narayana Rao, D., Furumoto, J., and Tsuda, T.:
726 Development of radio acoustic sounding system (RASS) with Gadanki MST radar
727 – first results, Ann. Geophys., 26, 2531-2542, doi:
728 10.5194/angeo-26-2531-2008, 2008.

729 Ecklund, W. L., Carter, D. A., and Balsley, B. B.: A UHF wind profiler for the
730 boundary layer: Brief description and initial results, J. Atmos. Oceanic Technol., 5,
731 432-441, doi: 10.1175/1520-0426(1988)005<0432:AUWPFT>2.0.CO;2, 1988.

732 Fukao, S., Sato, T., Tsuda, T., Kato, S., Wakasugi, K., and Makihira, T.: The MU radar
733 with an active phased array system: 1. Antenna and power amplifiers, Radio Sci.,
734 20, 1155-1168, doi: 10.1029/RS020i006p01155, 1985.

735 Gan, W.-S., Yang, J., and Kamakura, T.: A review of parametric acoustic array in air,
736 Appl. Acoust., 73, 1211-1219, doi: 10.1016/j.apacoust.2012.04.001, 2012.

737 Grdsdorf, U. and Lehmann, V.: Enhanced accuracy of RASS-measured temperatures
738 due to an improved range correction, J. Atmos. Oceanic Technol., 17, 406-416, doi:
739 10.1175/1520-0426(2000)017<0406:Eaormt>2.0.Co;2, 2000.

740 Hashiguchi, H., Fukao, S., Moritani, Y., Wakayama, T., and Watanabe, S.: A lower
741 troposphere radar: 1.3-GHz active phased-array type wind profiler with RASS, J.
742 Meteor. Soc. Japan, 82, 915-931, doi: 10.2151/jmsj.2004.915, 2004.

743 Health Canada: Guidelines for the safe use of ultrasound: Part II Industrial and
744 commercial applications, Safety Code 24, available online at:
745 [http://www.hc-sc.gc.ca/ewh-semt/alt_formats/hecs-sesc/pdf/pubs/radiation/safety-c
747 ode_24-securite/safety-code_24-securite-eng.pdf](http://www.hc-sc.gc.ca/ewh-semt/alt_formats/hecs-sesc/pdf/pubs/radiation/safety-c

746 ode_24-securite/safety-code_24-securite-eng.pdf), Minister of supply and services
748 Canada, 1991.

748 Ishihara, M., Kato, Y., Abo, T., Kobayashi, K., and Izumikawa, Y.: Characteristics and
749 performance of the operational wind profiler network of the Japan Meteorological
750 Agency, J. Meteor. Soc. Japan, 84, 1085-1096, doi: 10.2151/jmsj.84.1085, 2006.

751 ISO: 9613-1, Acoustics - Attenuation of sound during propagation outdoors - Part 1:
752 Calculation of the absorption of sound by the atmosphere, available online at:
753 <https://www.iso.org/standard/17426.html>, 30pp, 1993.

754 ISO: 9613-2, Acoustics - Attenuation of sound during propagation outdoors - Part 2:
755 General method of calculation, 1996. 18pp, 1996.

756 Johnston, P. E., Hartten, L. M., Love, C. H., Carter, D. A., and Gage, K. S.: Range
757 errors in wind profiling caused by strong reflectivity gradients, *J. Atmos. Oceanic*
758 *Technol.*, 19, 934-953, doi:
759 10.1175/1520-0426(2002)019<0934:REIWPC>2.0.CO;2, 2002.

760 Kizu, N., Sugidachi, T., Kobayashi, E., Hoshino, S., Shimizu, K., Maeda, R., and
761 Fujiwara, M.: Technical characteristics and GRUAN data processing for the Meisei
762 RS-11G and iMS-100 radiosondes, GRUAN-TD-5, GRUAN Lead Centre, 2018.

763 Lataitis, R. J.: Signal power for radio acoustic sounding of temperature: The effects of
764 horizontal winds, turbulence, and vertical temperature gradients, *Radio Sci.*, 27,
765 369-385, doi: doi:10.1029/92RS00004, 1992.

766 Law, D. C., McLaughlin, S. A., Post, M. J., Weber, B. L., Welsh, D. C., Wolfe, D. E.,
767 and Merritt, D. A.: An electronically stabilized phased array system for shipborne
768 atmospheric wind profiling, *J. Atmos. Oceanic Technol.*, 19, 924-933, doi:
769 10.1175/1520-0426(2002)019<0924:AESPAS>2.0.CO;2, 2002.

770 Marshall, J. M., Peterson, A. M., and Barnes, A. A.: Combined Radar-Acoustic
771 Sounding System, *Applied Optics*, 11, 108-112, doi: 10.1364/AO.11.000108, 1972.

772 Martner, B. E., Wuertz, D. B., Stankov, B. B., Strauch, R. G., Westwater, E. R., Gage,
773 K. S., Ecklund, W. L., Martin, C. L., and Dabberdt, W. F.: An evaluation of wind
774 profiler, RASS, and microwave radiometer performance, *Bull. Amer. Meteor. Soc.*,
775 74, 599-614, doi: 10.1175/1520-0477(1993)074<0599:AEOWPR>2.0.CO;2, 1993.

776 Masuda, Y.: Influence of wind and temperature on the height limit of a radio acoustic
777 sounding system, *Radio Sci.*, 23, 647-654, doi: 10.1029/RS023i004p00647, 1988.

778 Matuura, N., Masuda, Y., Inuki, H., Kato, S., Fukao, S., Sato, T., and Tsuda, T.: Radio
779 acoustic measurement of temperature profile in the troposphere and stratosphere,
780 *Nature*, 323, 426, doi: 10.1038/323426a0, 1986.

781 May, P. T.: Thermodynamic and vertical velocity structure of two gust fronts observed
782 with a wind profiler/RASS during MCTEX, *Mon. Wea. Rev.*, 127, 1796-1807, doi:
783 10.1175/1520-0493(1999)127<1796:TAVVSO>2.0.CO;2, 1999.

784 May, P. T., Moran, K. P., and Strauch, R. G.: The accuracy of RASS temperature
785 measurements, *J. Appl. Meteor*, 28, 1329-1335, doi:
786 10.1175/1520-0450(1989)028<1329:Taortm>2.0.Co;2, 1989.

787 May, P. T., Strauch, R. G., and Moran, K. P.: The altitude coverage of temperature
788 measurements using RASS with wind profiler radars, *Geophys. Res. Lett.*, 15,
789 1381-1384, doi: 10.1029/GL015i012p01381, 1988.

790 Moran, K. P. and Strauch, R. G.: The accuracy of RASS temperature measurements
791 corrected for vertical air motion, *J. Atmos. Oceanic Technol.*, 11, 995-1001, doi:
792 10.1175/1520-0426(1994)011<0995:TAORTM>2.0.CO;2, 1994.

793 Moran, K. P., Wuertz, D. B., Strauch, R. G., Abshire, N. L., and Law, D. C.:
794 Temperature sounding with wind profiler radars, *J. Atmos. Oceanic Technol.*, 8,
795 606-608, doi: 10.1175/1520-0426(1991)008<0606:Tswwpr>2.0.Co;2, 1991.

796 Neiman, P. J., May, P. T., and Shapiro, M. A.: Radio acoustic sounding system (RASS)
797 and wind profiler observations of lower- and midtropospheric weather systems,
798 *Mon. Wea. Rev.*, 120, 2298-2313, doi:
799 10.1175/1520-0493(1992)120<2298:RASSAW>2.0.CO;2, 1992.

800 Palmer, R. D., Cheong, B. L., Hoffman, M. W., Frasier, S. J., and López-Dekker, F. J.:
801 Observations of the small-scale variability of precipitation using an imaging radar,
802 *J. Atmos. Oceanic Technol.*, 22, 1122-1137, doi: 10.1175/JTECH1775.1, 2005.

803 Peters, G., Hinzpeter, H., and Baumann, G.: Measurements of heat flux in the
804 atmospheric boundary layer by sodar and RASS: A first attempt, *Radio Sci.*, 20,
805 1555-1564, doi: 10.1029/RS020i006p01555, 1985.

806 Peters, G. and Kirtzel, H. J.: Measurements of Momentum Flux in the Boundary Layer
807 by RASS, *J. Atmos. Oceanic Technol.*, 11, 63-75, doi:
808 10.1175/1520-0426(1994)011<0063:Momfit>2.0.Co;2, 1994.

809 Westervelt, P. J.: Parametric Acoustic Array, *J. Acoust. Soc. Am.*, 35, 535-537, doi:
810 10.1121/1.1918525, 1963.

811 White, A. B., Neiman, P. J., Ralph, F. M., Kingsmill, D. E., and Persson, P. O. G.:
812 Coastal orographic rainfall processes observed by radar during the California
813 Land-Falling Jets Experiment, *J. Hydrometeor.*, 4, 264-282, doi:
814 10.1175/1525-7541(2003)4<264:CORPOB>2.0.CO;2, 2003.

815 WHO: Environmental Health Criteria for ultrasound, available online at:
816 <http://www.inchem.org/documents/ehc/ehc/ehc22.htm>, Environmental Health
817 Criteria 22, 1982.

818 WMO: GCOS Reference Upper-Air Network (GRUAN): Justification, requirements,
819 siting and instrumentation options, GCOS-112, WMO/TD 1379, 2007.

820 Wu, S., Wu, M., Huang, C., and Yang, J.: FPGA-based implementation of steerable
821 parametric loudspeaker using fractional delay filter, *Appl. Acoust.*, 73, 1271-1281,
822 doi: 10.1016/j.apacoust.2012.04.013, 2012.

823 Wulfmeyer, V., Hardesty, R. M., Turner, D. D., Behrendt, A., Cadeddu, M. P., Di
824 Girolamo, P., Schlüssel, P., Van Baelen, J., and Zus, F.: A review of the remote
825 sensing of lower tropospheric thermodynamic profiles and its indispensable role for
826 the understanding and the simulation of water and energy cycles, *Rev. Geophys.*,
827 53, 819-895, doi: 10.1002/2014RG000476, 2015.

828

829

List of Tables

830 Table 1. Parameters of the wind profiler with RASS.

831 Table 2. Characteristics of the MRI parametric speaker.

832 Table 3. List of the comparison experiments, including date, period, sea level

833 pressure, surface temperature, surface wind speed, and mean wind speed

834 aloft (20 — 1200 m AGL).

835

836

List of Figures

837 Figure 1. Pictures of (a) LAP-3000 with acoustic speakers and a parametric speaker for

838 RASS, (b) top view, (c) partial expanded view of the parametric speaker, and (d) rotary

839 warning lights on the shed wall. The parametric speaker mounted on top of the shed

840 with a sliding roof is covered with rainproof film in the field, as shown in (a).

841

842 Figure 2. Audible sound pressure level (SPL) pattern for an acoustic speaker (red), the

843 parametric speaker with the measured beam width of 5° (blue) and 12° (black) at a

844 frequency of 3 kHz. The error bars represent 2σ . The SPL pattern for the acoustic

845 speaker in the negative zenith angle region is a mirror image of the pattern measured at

846 the positive zenith angle for ease of viewing. The background noise level was about 50
847 dB. The SPL was measured with a sound level meter (Rion NL-42).

848

849 Figure 3. Profiles of atmospheric-attenuation coefficient α and atmospheric attenuation
850 for sound at frequencies of (a) 3 kHz and (b) 40 kHz derived from the radiosonde
851 measurements at 08:30 JST on 19 October 2016, at the MRI site.

852

853 Figure 4. Doppler spectra from RASS observations measured with (a) acoustic speakers
854 from 08:30 JST for 1 min and (b) the parametric speaker from 08:31 JST for 1 min on
855 19 October 2016. At each height, the first moment of the spectrum, indicated by the
856 vertical bar, gives the vertical sound velocity, and the second moment, indicated by the
857 horizontal bar, gives the spectral width.

858

859 Figure 5. Profiles of received mean RASS echo power, horizontal displacement of the
860 parametric speaker sound from radio wave, and wind speed on (a) 19 October 2016, (b)
861 27 October 2016, (c) 9 August 2017, and (d) 7 September 2017, derived with the

862 acoustic speakers (red), the parametric speaker (blue), and radiosonde (green). The error
863 bars represent 2σ . The black lines indicate linear regressions for the received power data
864 (except for the first range) as shown in the upper-right legend with correlation
865 coefficients.

866

867 Figure 6. Profiles of virtual temperature (T_v) and received power (P_r) from 08:30 JST
868 on (a) 15 October, (b) 21 October, (c) 8 November, and (d) 30 November 2016 derived
869 from a radiosonde (black), RASS with acoustic speakers (red and orange), and the
870 parametric speaker (blue). The radiosonde data were smoothed by 100 m running means
871 to match with the vertical resolution of the RASS. The error bars represent 2σ in the
872 RASS hourly observations. The mean, standard deviation, and number of samples of
873 temperature difference are summarized in a table in each panel.

874

875 Figure 7. Scatterplots of virtual temperature of the RASS vs. the radiosonde
876 measurements at all heights except for the first range. The data derived from the RASS
877 with the acoustic speakers (the parametric speaker) are plotted as open (closed) circles.

878 The radiosonde data were smoothed by 100 m running means to match with the vertical
879 resolution of RASS. The lines represent linear regressions for each data set as shown in
880 an upper legend along with the correlation coefficients. The mean, standard deviation
881 and number of samples of temperature difference are summarized in a bottom table.

882

883 Figure 8. Profiles of the virtual temperature (T_v) from 08:30 JST on 7 September 2017,
884 derived from a radiosonde (black), RASS with acoustic speakers (red), with the
885 parametric speaker (blue), and horizontal displacement of the radiosonde from the
886 profiler (green). The radiosonde data were smoothed by 100 m running means to match
887 with the vertical resolution of RASS. The error bars represent 2σ in the RASS
888 observations averaged over 60 min, and closed circles represent 1 min raw data from the
889 time indicated. The mean, standard deviation, and number of samples of temperature
890 difference of RASS from radiosonde are summarized in the table.

891

892 Figure 9. Comparisons of the parametric speaker vs. the acoustic speakers in measuring
893 virtual temperature at all heights (except for the first gate) shown by (a) a normalized

894 frequency diagram (color scale) and (b) a scatterplot. The data obtained from each
895 speaker system every 1 min alternately were used in (a), whereas the hourly-mean data
896 were plotted in (b). The mean T_v derived with the acoustic speakers is shifted 10°C for
897 ease of viewing in (b). The lines represent linear regressions for each data set, shown in
898 the upper-left and lower-right legends along with correlation coefficients, respectively.
899 The mean, standard deviation, and number of samples of temperature difference are
900 summarized in each table.

901

902 Figure 10. Scatterplots of mean height coverage of RASS measurement vs. horizontal
903 displacement of the beam center of the sound for RASS from that of the radio wave at
904 1200 m AGL derived from radiosonde observations. Closed circles (squares) denote the
905 observed mean RASS height coverage by acoustic speakers (parametric speaker) with
906 standard deviations indicated by error bars. The color scale represents the mean wind
907 speed aloft (20–1200 m AGL). Thick lines represent linear regressions for each data set,
908 where the PAA data are divided by a height threshold of 1100 m AGL. The highest
909 range gate sampled for the RASS measurement is 1300 m AGL.

910

911 Figure 11. Audible sound pressure pattern of the parametric speaker at a frequency of 3
912 kHz measured at multiple zenith angles, shown in the upper legend with the beam width
913 observed. Note that the peak SPL was decreased by about 7.5 dB for safety. The SPL
914 was measured with a sound level meter (Rion NL-42).

915

916 Figure A1. Simulated atmospheric-attenuation coefficients for sound at the frequencies
917 of (a) 3 kHz and (b) 40 kHz as a function of the atmospheric temperature and the
918 relative humidity at an atmospheric pressure of 1013 hPa. Results for a pressure of 900
919 hPa are also plotted for a relative humidity of 20%.

Table 1. Parameters of the wind profiler with RASS.

Frequency	1357.5 MHz
Peak Power	500 W
Beam width	< 7°
Beam elevation	90°
Pulse width	665 ns
First range gate	200 m
Last range gate	1300 m
Gate spacing	100 m
Interpulse period	12163 ns
Coherent Integration	3
Spectra Averaged	191
Number of FFT points	8192
Acoustic source	Pseudo-random frequencies (random hop)
Location	36°03'19"N, 140°07'28"E
Manufacture	Scintec
Model	LAP-3000

Table 2. Characteristics of the MRI parametric speaker.

Center frequency	40.0±1.0 kHz
Band width (-6dB)	< 2.0 kHz
Sound pressure level	> 200 dB (at 0.3m, 40 kHz, theoretical value)
Number of transducers	10008
Number of channels	278
Beam width	5°—17° (1° step)
Beam elevation	60—90° (1° step)
Beam azimuth	0—359° (1° step)
Input audio signal freq.	2.8—3.3 kHz
Speaker diameter	1.8 m
Speaker system size	2.1 x 2.1 x 1.8 m
Manufacture	Starlite Co., Ltd.
Model	100FM-001

Table 3. List of the comparison experiments, including date, period, sea level pressure, surface temperature, surface wind speed, and mean wind speed aloft (20 – 1200 m AGL).

Date	Time [JST]	P_{sea} [hPa]	T [°C]	U [m s ⁻¹]	$\overline{U}_{\text{aloft}}$ [m s ⁻¹]
14 Oct. 2016	0803–0900	1023.0	15.0	2.0	5.8±2.8
15 Oct. 2016	0801–0900	1025.5	15.8	1.4	2.1±0.5
19 Oct. 2016	0801–0900	1015.6	20.2	3.1	5.4±1.7
21 Oct. 2016	0801–0900	1016.5	15.7	2.1	3.1±0.7
24 Oct. 2016	0819–0900	1014.9	13.1	2.0	3.2±1.5
27 Oct. 2016	0837–0932	1016.1	18.8	0.8	1.6±0.6
28 Oct. 2016	0803–0900	1018.4	12.5	1.2	7.6±3.3
31 Oct. 2016	0809–0900	1024.3	12.7	1.7	5.4±2.6
02 Nov. 2016	0825–0902	1023.2	9.8	1.6	5.0±2.3
08 Nov. 2016	0803–0902	1017.0	7.4	2.2	5.4±3.4
12 Nov. 2016	0809–0906	1019.8	11.8	0.4	3.7±1.3
30 Nov. 2016	0911–0932	1030.4	5.7	1.8	2.9±1.4
29 Mar. 2017	0843–0900	1020.0	8.4	2.4	4.9±1.3
09 Aug. 2017	0845–0900	991.3	30.5	1.2	4.5±2.5
07 Sep. 2017	0801–0900	1003.2	22.3	1.8	2.3±0.5
09 Apr. 2018	0825–0902	1013.6	10.2	1.6	6.9±5.1



Figure 1. Pictures of (a) LAP-3000 with acoustic speakers and a parametric speaker for RASS, (b) top view, (c) partial expanded view of the parametric speaker, and (d) rotary warning lights on the shed wall. The parametric speaker mounted on top of the shed with a sliding roof is covered with rainproof film in the field, as shown in (a).

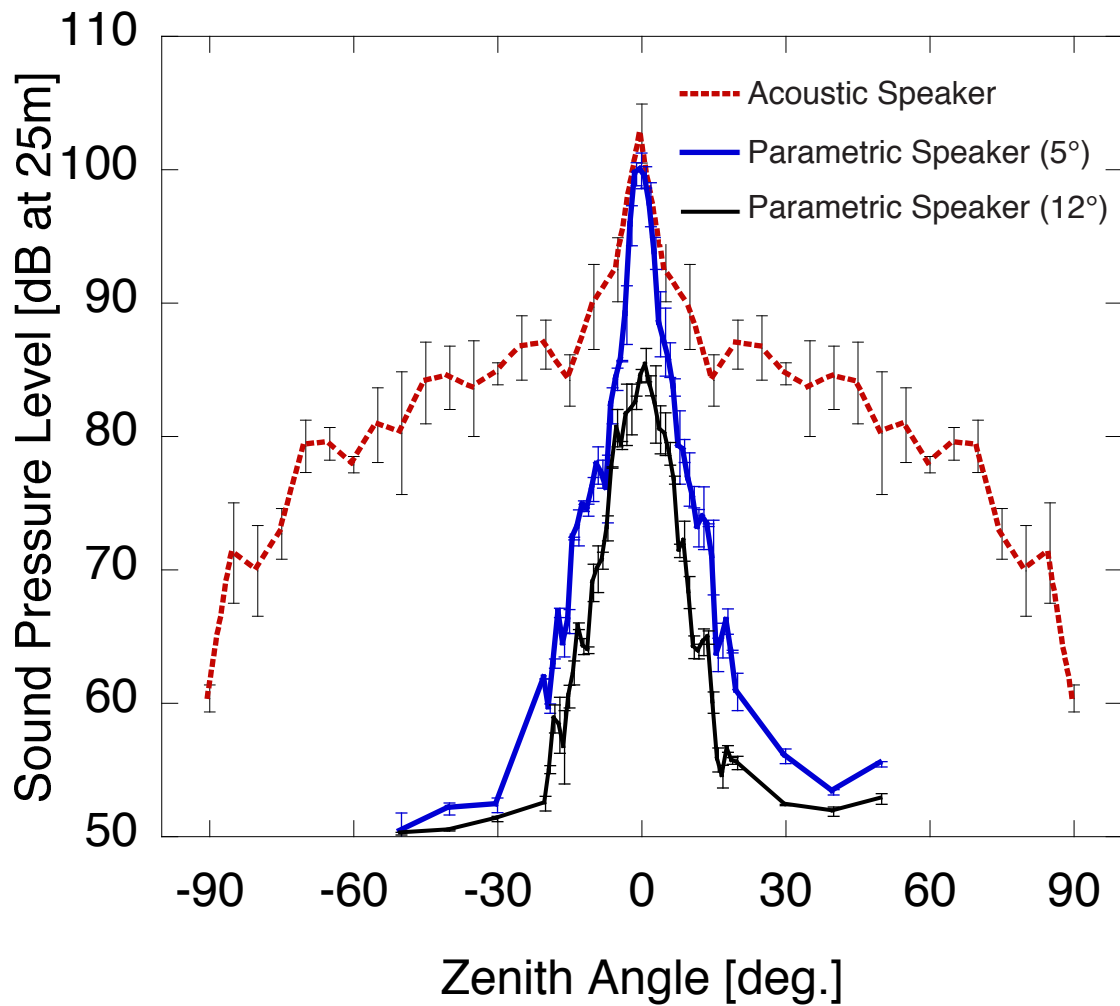


Figure 2. Audible sound pressure level (SPL) pattern for an acoustic speaker (red), the parametric speaker with the measured beam width of 5° (blue) and 12° (black) at a frequency of 3 kHz. The error bars represent 2σ . The SPL pattern for the acoustic speaker in the negative zenith angle region is a mirror image of the pattern measured at the positive zenith angle for ease of viewing. The background noise level was about 50 dB. The SPL was measured with a sound level meter (Rion NL-42).

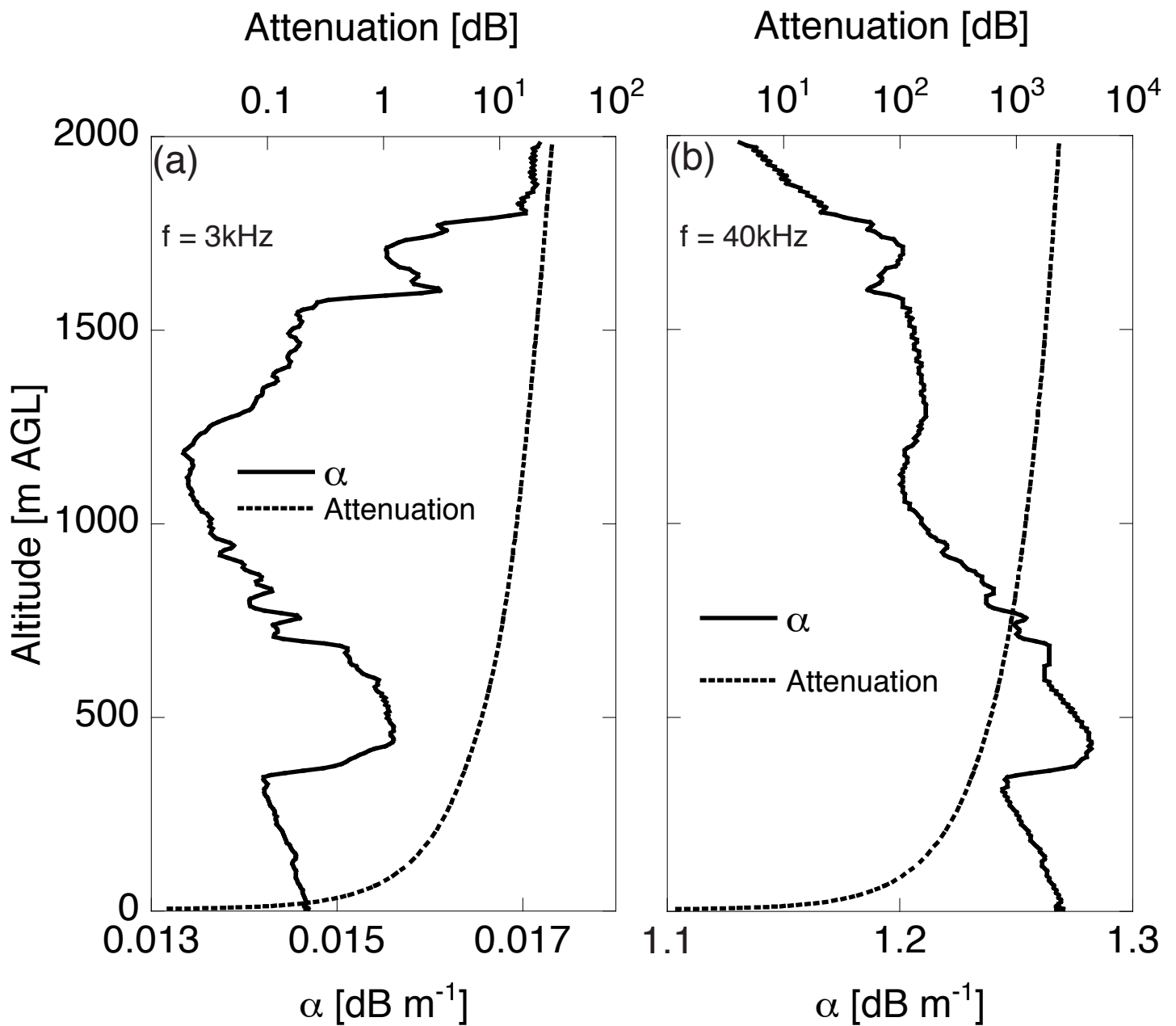


Figure 3. Profiles of atmospheric-attenuation coefficient α and atmospheric attenuation for sound at frequencies of (a) 3 kHz and (b) 40 kHz derived from the radiosonde measurements at 08:30 JST on 19 October 2016, at the MRI site.

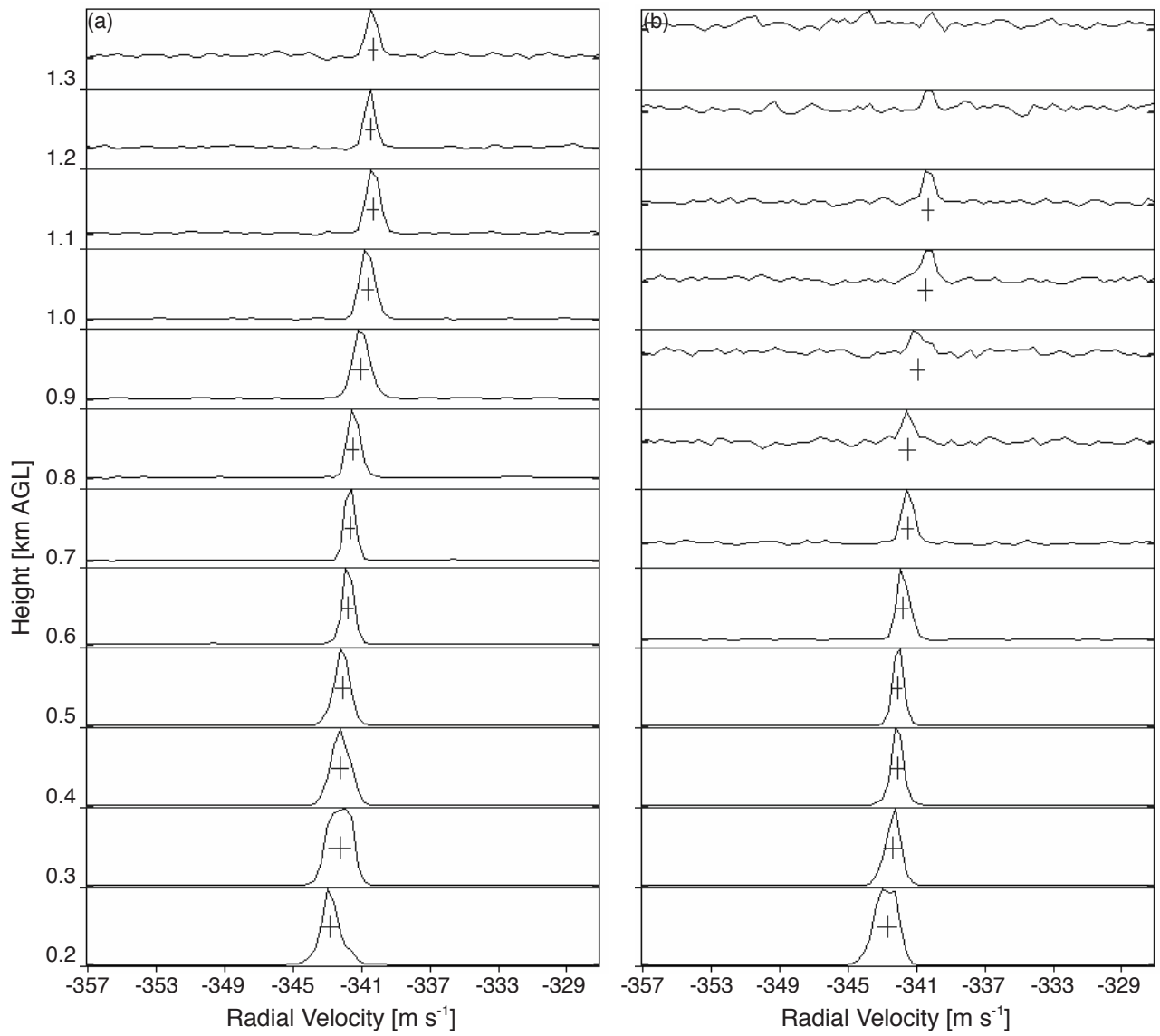


Figure 4. Doppler spectra from RASS observations measured with (a) acoustic speakers from 08:30 JST for 1 min and (b) the parametric speaker from 08:31 JST for 1 min on 19 October 2016. At each height, the first moment of the spectrum, indicated by the vertical bar, gives the vertical sound velocity, and the second moment, indicated by the horizontal bar, gives the spectral width.

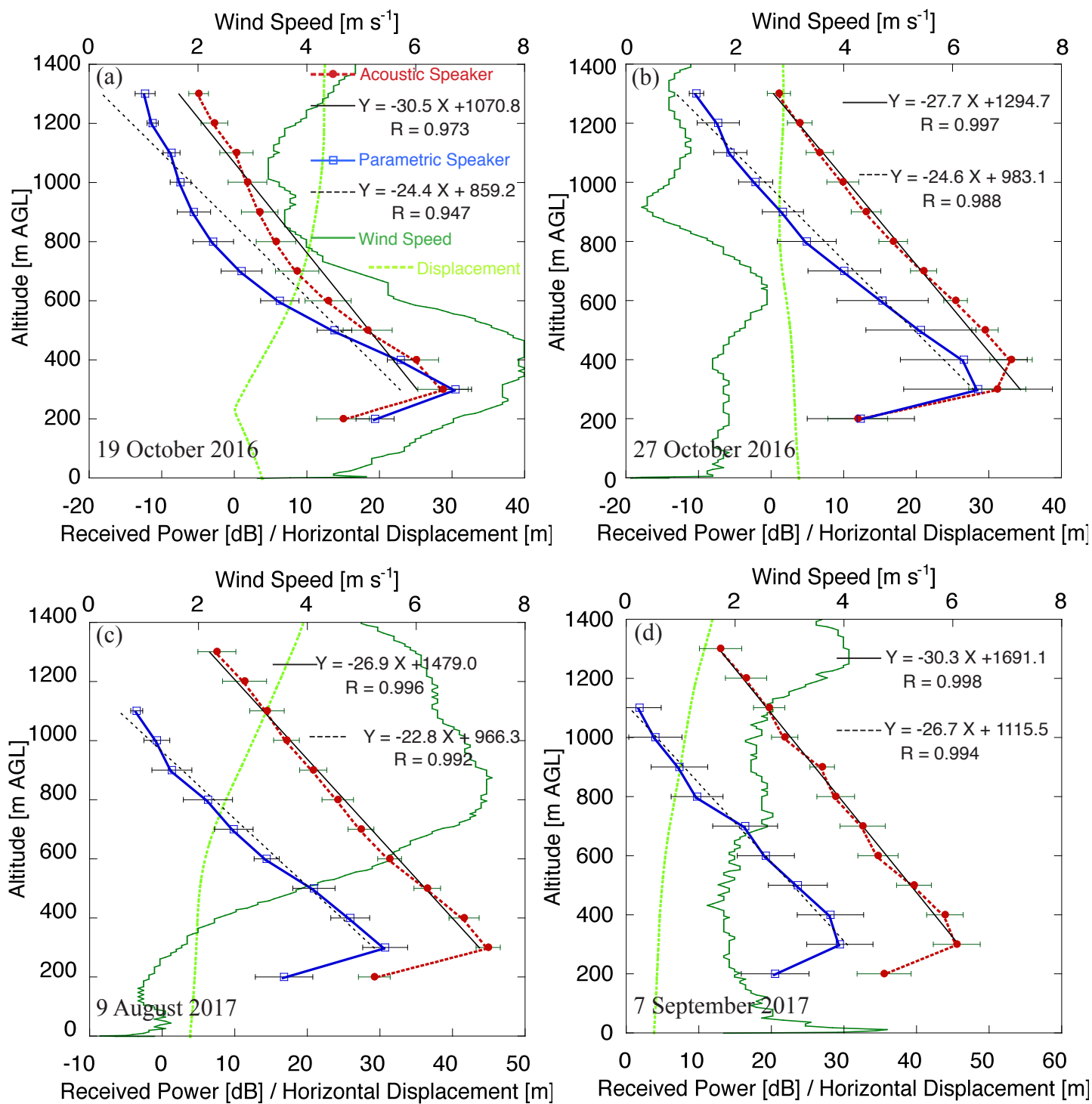


Figure 5. Profiles of received mean RASS echo power, horizontal displacement of the parametric speaker sound from radio wave, and wind speed on (a) 19 October 2016, (b) 27 October 2016, (c) 9 August 2017, and (d) 7 September 2017, derived with the acoustic speakers (red), the parametric speaker (blue), and radiosonde (green). The error bars represent 2σ . The black lines indicate linear regressions for the received power data (except for the first range) as shown in the upper-right legend with correlation coefficients.

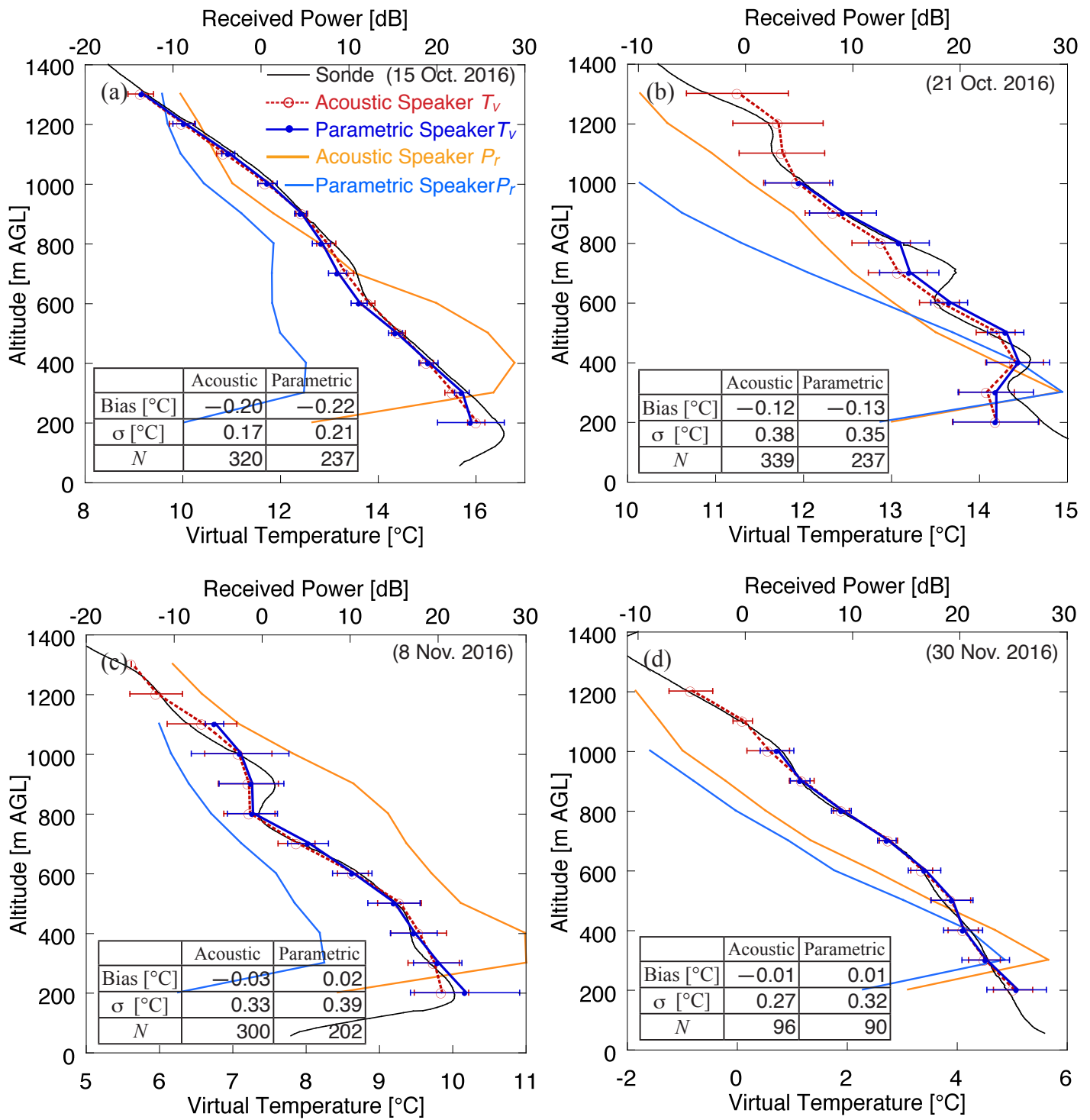


Figure 6. Profiles of virtual temperature (T_v) and received power (P_r) from 08:30 JST on (a) 15 October, (b) 21 October, (c) 8 November, and (d) 30 November 2016 derived from a radiosonde (black), RASS with acoustic speakers (red and orange), and the parametric speaker (blue). The radiosonde data were smoothed by 100 m running means to match with the vertical resolution of the RASS. The error bars represent 2σ in the RASS hourly observations. The mean, standard deviation, and number of samples of temperature difference are summarized in a table in each panel.

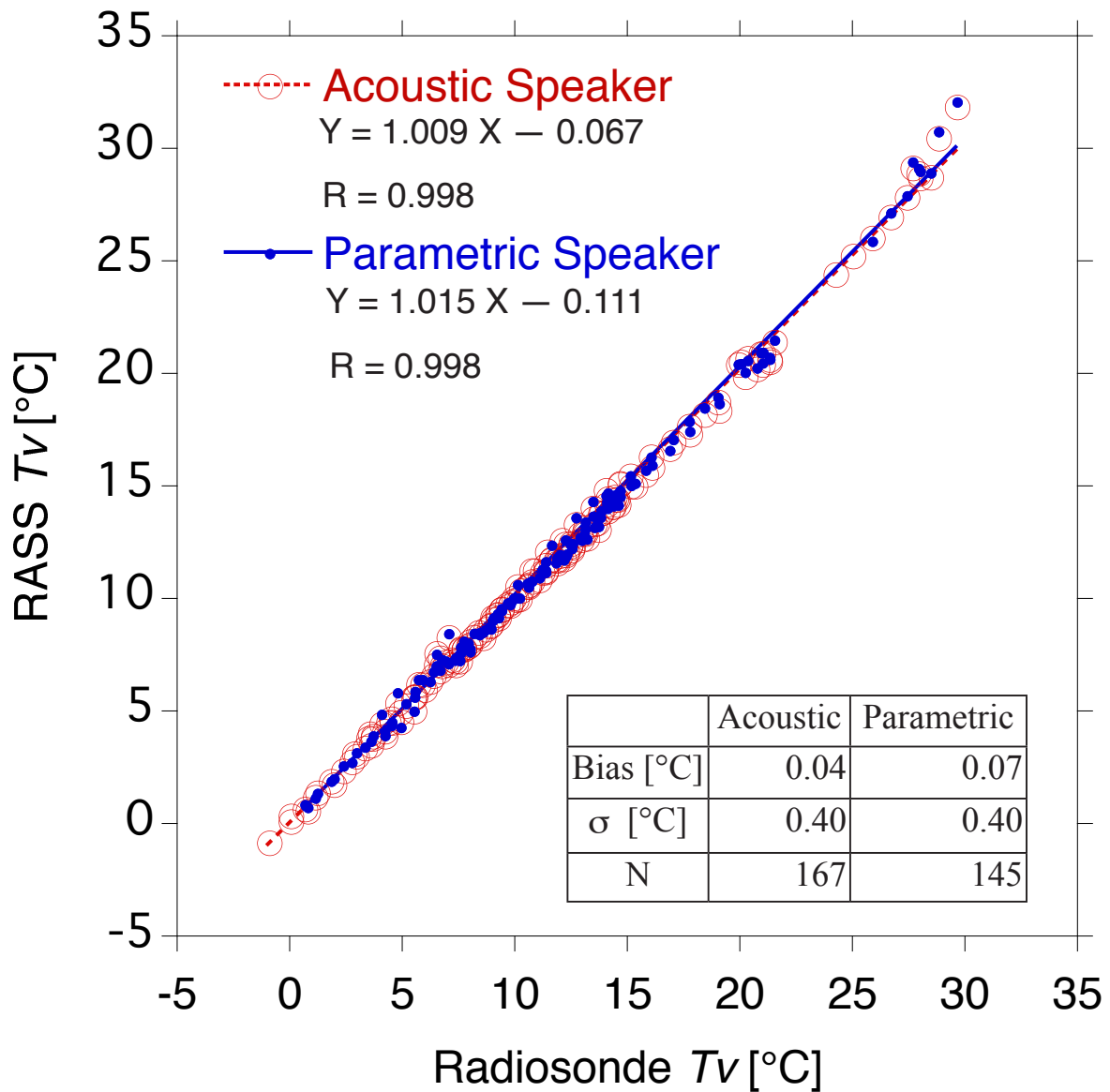


Figure 7. Scatterplots of virtual temperature of the RASS vs. the radiosonde measurements at all heights except for the first range. The data derived from the RASS with the acoustic speakers (the parametric speaker) are plotted as open (closed) circles. The radiosonde data were smoothed by 100 m running means to match with the vertical resolution of RASS. The lines represent linear regressions for each data set as shown in an upper legend along with the correlation coefficients. The mean, standard deviation and number of samples of temperature difference are summarized in a bottom table.

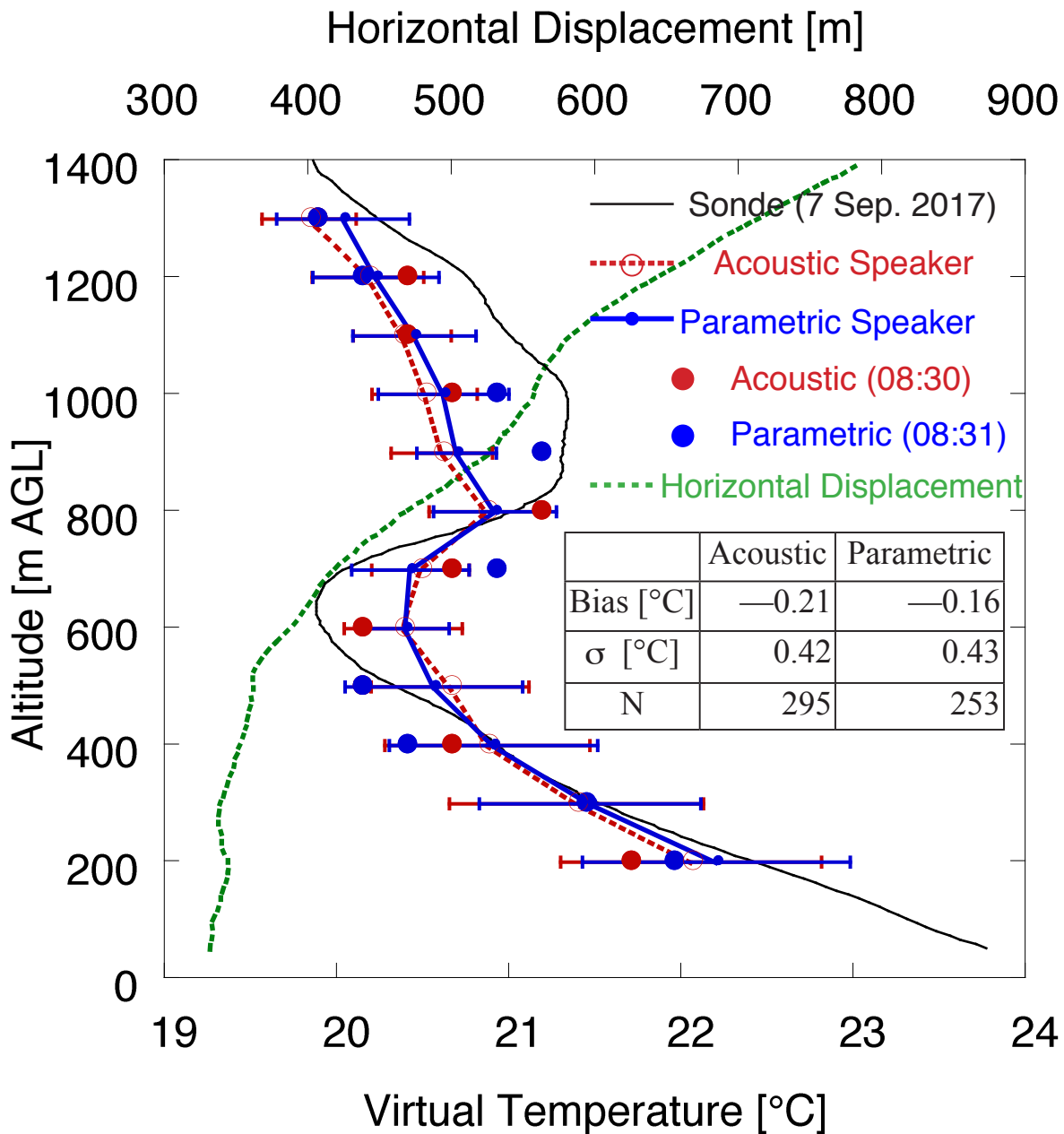


Figure 8. Profiles of the virtual temperature (T_v) from 08:30 JST on 7 September 2017, derived from a radiosonde (black), RASS with acoustic speakers (red), with the parameter speaker (blue), and horizontal displacement of the radiosonde from the profiler (green). The radiosonde data were smoothed by 100 m running means to match with the vertical resolution of RASS. The error bars represent 2σ in the RASS observations averaged over 60 min, and closed circles represent 1 min raw data from the time indicated. The mean, standard deviation, and number of samples of temperature difference of RASS from radiosonde are summarized in the table.

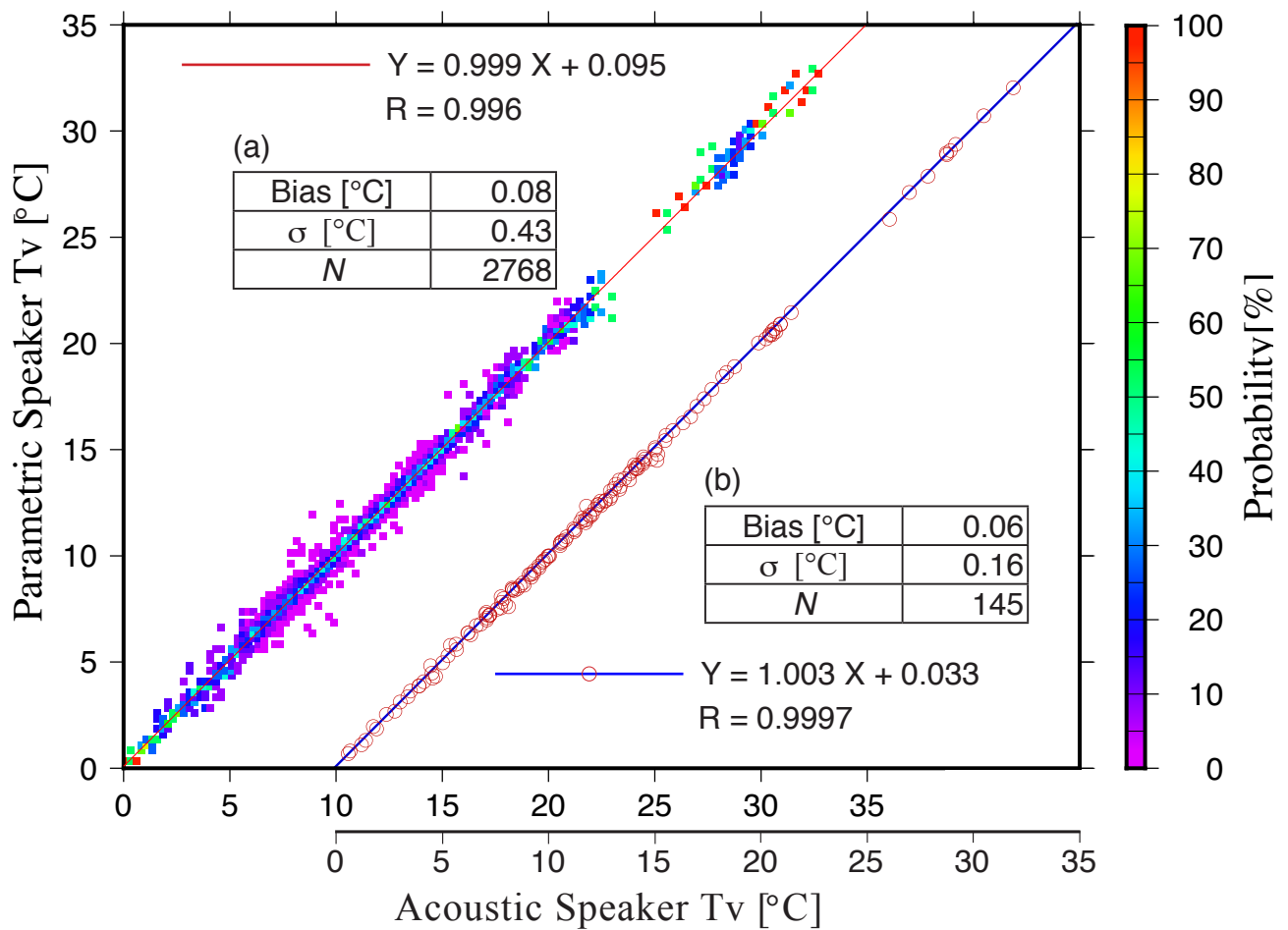


Figure 9. Comparisons of the parametric speaker vs. the acoustic speakers in measuring virtual temperature at all heights (except for the first gate) shown by (a) a normalized frequency diagram (color scale) and (b) a scatterplot. The data obtained from each speaker system every 1 min alternately were used in (a), whereas the hourly-mean data were plotted in (b). The mean T_v derived with the acoustic speakers is shifted 10°C for ease of viewing in (b). The lines represent linear regressions for each data set, shown in the upper-left and lower-right legends along with correlation coefficients, respectively. The mean, standard deviation, and number of samples of temperature difference are summarized in each table.

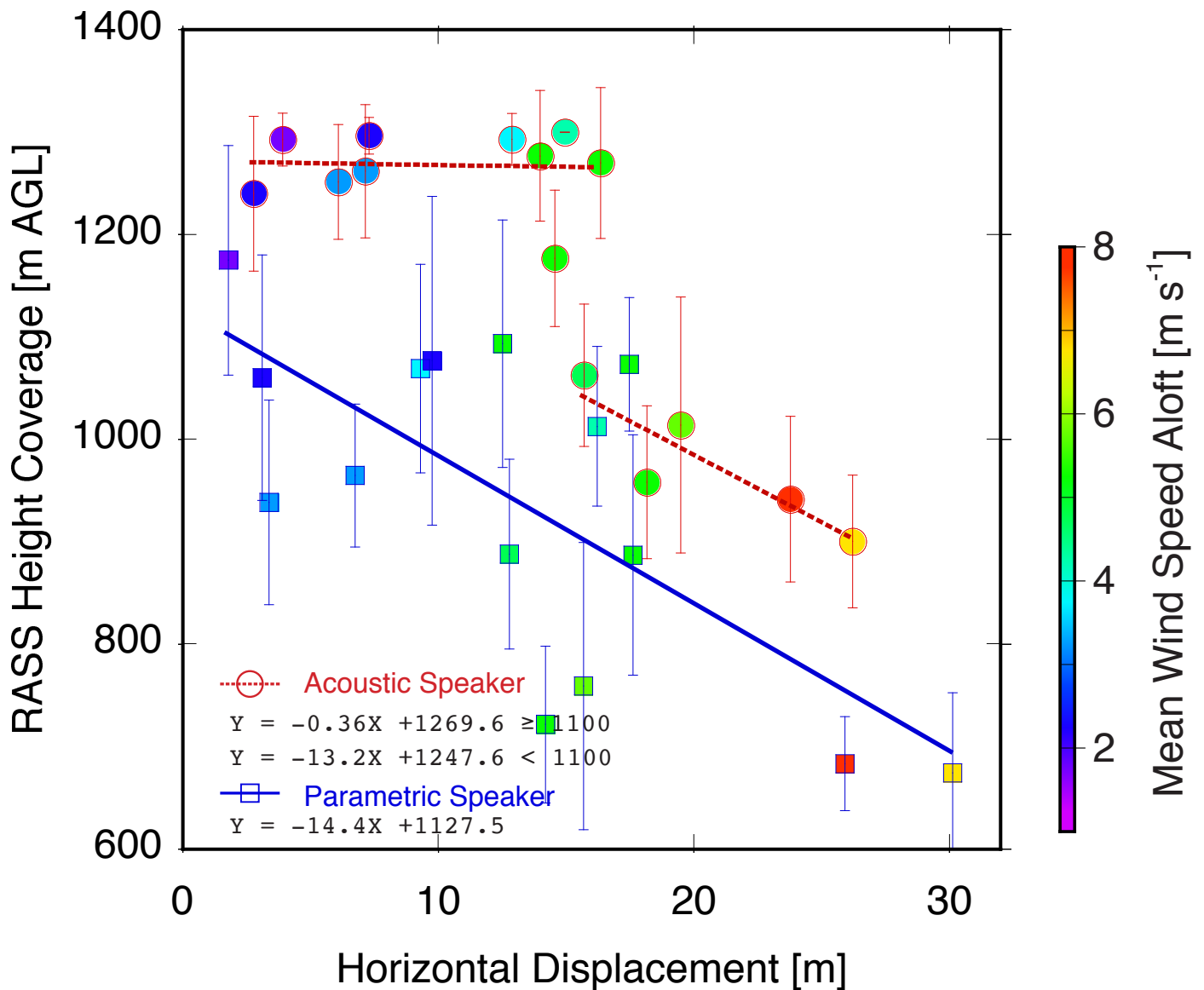


Figure 10. Scatterplots of mean height coverage of RASS measurement vs. horizontal displacement of the beam center of the sound for RASS from that of the radio wave at 1200 m AGL derived from radiosonde observations. Closed circles (squares) denote the observed mean RASS height coverage by acoustic speakers (parametric speaker) with standard deviations indicated by error bars. The color scale represents the mean wind speed aloft (20–1200 m AGL). Thick lines represent linear regressions for each data set, where the PAA data are divided by a height threshold of 1100 m AGL. The highest range gate sampled for the RASS measurement is 1300 m AGL.

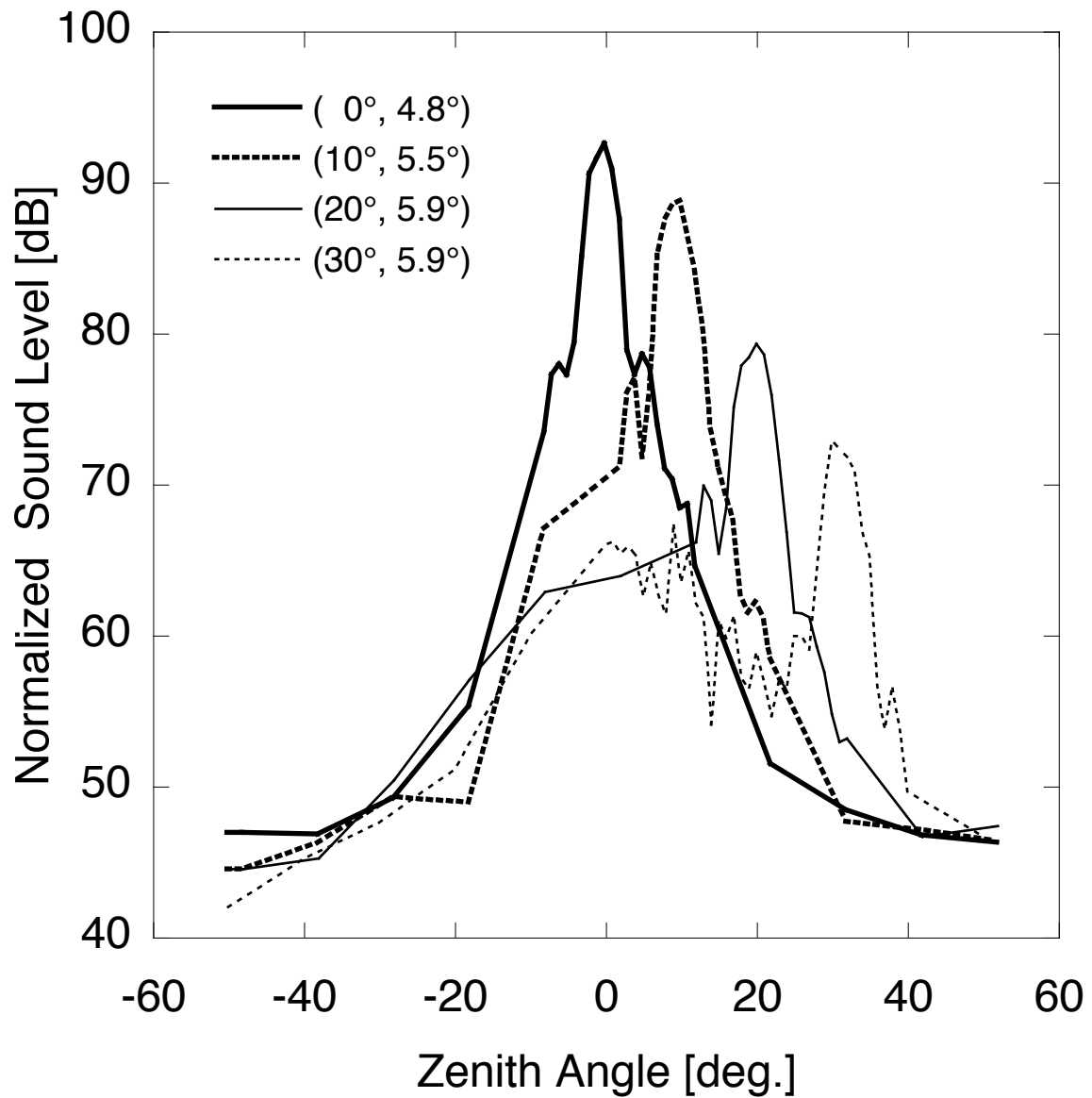


Figure 11. Audible sound pressure pattern of the parametric speaker at a frequency of 3 kHz measured at multiple zenith angles, shown in the upper legend with the beam width observed. Note that the peak SPL was decreased by about 7.5 dB for safety. The SPL was measured with a sound level meter (Rion NL-42).

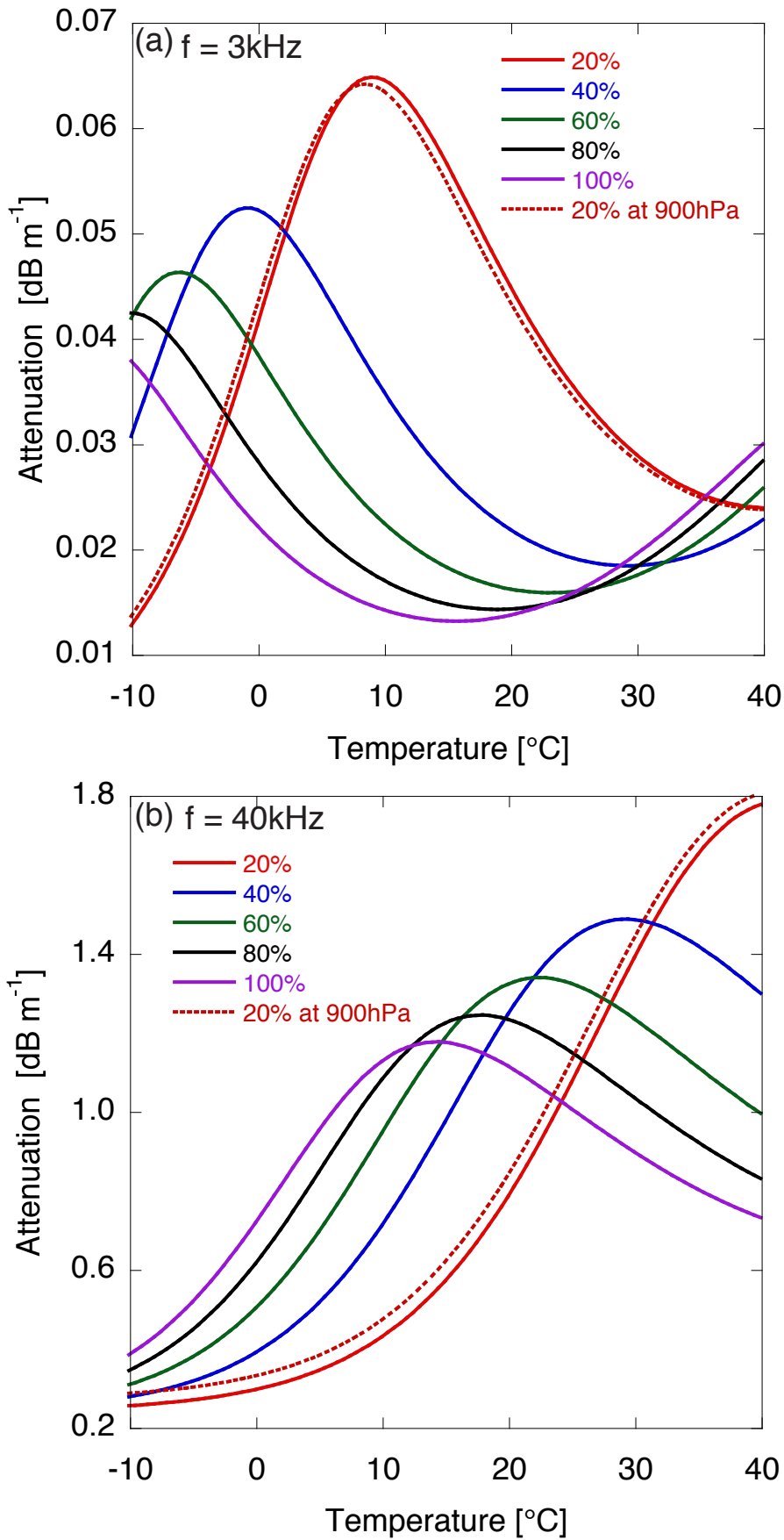


Figure A1. Simulated atmospheric-attenuation coefficients for sound at the frequencies of (a) 3 kHz and (b) 40 kHz as a function of the atmospheric temperature and the relative humidity at an atmospheric pressure of 1013 hPa. Results for a pressure of 900 hPa are also plotted for a relative humidity of 20%.